



Unstable Resonator Mid-Infrared Laser Sources

**Steven Brueck
UNIVERSITY OF NEW MEXICO**

**02/26/2016
Final Report**

DISTRIBUTION A: Distribution approved for public release.

**Air Force Research Laboratory
AF Office Of Scientific Research (AFOSR)/ RTB1
Arlington, Virginia 22203
Air Force Materiel Command**

REPORT DOCUMENTATION PAGE

Form Approved
OMB No. 0704-0188

The public reporting burden for this collection of information is estimated to average 1 hour per response, including the time for reviewing instructions, searching existing data sources, gathering and maintaining the data needed, and completing and reviewing the collection of information. Send comments regarding this burden estimate or any other aspect of this collection of information, including suggestions for reducing the burden, to Department of Defense, Washington Headquarters Services, Directorate for Information Operations and Reports (0704-0188), 1215 Jefferson Davis Highway, Suite 1204, Arlington, VA 22202-4302. Respondents should be aware that notwithstanding any other provision of law, no person shall be subject to any penalty for failing to comply with a collection of information if it does not display a currently valid OMB control number.
PLEASE DO NOT RETURN YOUR FORM TO THE ABOVE ADDRESS.

1. REPORT DATE (DD-MM-YYYY) 02/12/2016	2. REPORT TYPE Final	3. DATES COVERED (From - To) 09/30/2012-09/29/2015
--	--------------------------------	--

4. TITLE AND SUBTITLE Unstable Resonator Mid-Infrared Laser Sources	5a. CONTRACT NUMBER
	5b. GRANT NUMBER FA9550-12-1-0480
	5c. PROGRAM ELEMENT NUMBER

6. AUTHOR(S) Steven R. J. Brueck	5d. PROJECT NUMBER
	5e. TASK NUMBER
	5f. WORK UNIT NUMBER

7. PERFORMING ORGANIZATION NAME(S) AND ADDRESS(ES) The Regents of the University of New Mexico	8. PERFORMING ORGANIZATION REPORT NUMBER
--	---

9. SPONSORING/MONITORING AGENCY NAME(S) AND ADDRESS(ES) Air Force Office of Scientific Research 875 N. Randolph St. Rm 3112 Arlington, VA 22203	10. SPONSOR/MONITOR'S ACRONYM(S)
	11. SPONSOR/MONITOR'S REPORT NUMBER(S)

12. DISTRIBUTION/AVAILABILITY STATEMENT

DISTRIBUTION A

13. SUPPLEMENTARY NOTES

14. ABSTRACT

Progress has been made in tunable infrared lasers and in novel epitaxial structures for next generation electronics. A tunable infrared laser based on a chirped grating distributed feedback structure and optical pumping has been demonstrated with an 80-nm tuning range at 3.1 micron and a linewidth of < 1nm. Novel nanowire geometries based on selective growth of heterogeneous materials on Si(001) substrates have been designed and initial demonstrations of growth have been undertaken.

15. SUBJECT TERMS

tunable infrared laser, distributed feedback lasers, chirped gratings, interferometric lithography, nanowire transistors, tunnel field-effect transistors, nanoscale epitaxial growth, nanowire bending, substreshold slope

16. SECURITY CLASSIFICATION OF:			17. LIMITATION OF ABSTRACT	18. NUMBER OF PAGES	19a. NAME OF RESPONSIBLE PERSON
a. REPORT	b. ABSTRACT	c. THIS PAGE			Professor Steven R. J. Brueck
U	U	U	UU	32	19b. TELEPHONE NUMBER (Include area code) 505-292-7800

Abstract:

Progress has been made in tunable infrared lasers and in novel epitaxial structures for next generation electronics. A novel tunable infrared laser based on a chirped grating distributed feedback structure and optical pumping has been demonstrated with an 80-nm tuning range at 3.1 μm and a linewidth of $< 1\text{nm}$. Novel nanowire geometries based on selective growth of heterogeneous materials on Si(001) substrates have been designed and initial demonstrations of growth have been undertaken.

Introduction

Significant progress has been made in two areas during the course of this work: 1) continuously tunable distributed feedback lasers based on chirped gratings, and 2) nanowire growth for next generation electronics. Details are presented below.

Wide-band Continuously Tunable DFB Lasers

The mid-infrared 3- to 5- μm atmospheric transmission window is important for remote sensing and spectroscopic applications because it contains many fingerprint molecular rotation-vibrational absorption lines, such as O-H stretch at 2.8 μm ; N-H stretch at $\sim 3\ \mu\text{m}$, C-H stretch at $\sim 3.3\ \mu\text{m}$. Spectroscopic applications typically require a continuous wave (CW), single-longitudinal-mode (SLM) and mode-hop-free, continuously tunable, narrow spectral linewidth, high-power laser source with good beam quality. In this work, involving a collaboration between UNM and AFRL, a unique implementation of tunable DFB laser for spectroscopic applications is introduced; this technique is broadly applicable independent of the wavelength range. The lasing material was grown at AFRL (Dr. R. Kaspi group); the chirped grating fabrication and characterization was carried out at UNM (Prof. S. R. J. Brueck group).

Various laser wavelength tuning mechanisms have been demonstrated for semiconductor lasers, for different purposes and with different technical approaches. Approaches to wavelength tuning include thermal/operation temperature tuning [1], variable cavity length with cantilever/piezo actuator driven end-mirror in vertical cavity surface emitting lasers (MEMS/VCSEL) [2], quantum Stark effect [3-5] wavelength tuning by varying bias voltage in inter-band cascade semiconductor lasers (ICLs) and others. Of course, one important category of wavelength tuning techniques uses the dispersion property of a diffraction grating to select the lasing wavelength. Well-known forms of tunable semiconductor lasers in this category include external cavity lasers [6-10], grating coupled sampled-reflector (GCSR) lasers, sampled-grating DBR (SGDBR) lasers [11-14], super-structure grating (SSG) DFB lasers [15-18], and selectable DFB laser arrays [19-22]. External cavity lasers usually consist of a linear gain section and an external diffraction grating which pivots around an axis to select different lasing wavelengths. GCSR and SGDBR lasers are very similar in the sense that both tune their output wavelength using a Vernier effect. The monolithic laser cavities of both types of lasers usually have two or more sections patterned with sampled gratings of different periods which possess comb-like

reflection spectra (a series of discrete reflection peaks). The refractive indices of these sections are independently adjusted by varying the bias or current which shifts the gratings' reflection combs. The output wavelength of the laser is the coincident wavelength corresponding to overlapped reflection comb teeth of different grating sections. A selectable DFB array is simply a group of individual DFB lasers with different grating periods for different lasing wavelengths fabricated on a single die, which are individually turned on and coupled out through a multi-mode coupler. To have continuous wavelength coverage, the output wavelength of each individual DFB laser is usually tuned through operating temperature variation.

All of these tunable lasers have their advantages and drawbacks for different applications. External cavity lasers are widely used both in research and industry for spectroscopic applications, especially with quantum cascade lasers (QCLs) thanks to their very wide continuous wavelength tunability and narrow spectral linewidth. The main issues with this type of laser are manufacturability and reliability given the requirements of precise alignment of moving micro parts as well as the challenging antireflection coating to cover a wide tuning range in the gain section. GCSR and SGDBR lasers are monolithic, rugged, and can be conveniently integrated with an amplifier to achieve relatively high output powers. Typically, their wavelength tuning is discontinuous, and the primary application is to wavelength division multiplexing (WDM) in telecommunication applications or optical integrated circuits. These lasers are less suitable for spectroscopic applications where continuous, monotonic tuning is desired. Selectable DFB arrays, combined with QCLs have been demonstrated for spectroscopic applications thanks to their very wide wavelength tuning range. Normally e-beam grating patterning in GCSR/SGDBR and selectable DFB array lasers makes fabrication complicated and yield low. Wavelength tuning is also very complicated in both types of lasers because individual electronic circuitry is required for section bias/current control as well as operating temperature control.

In pursuit of a spectroscopic/remote sensing solution that combines the continuous tuning of an external cavity laser with the ruggedness and compactness of a monolithic grating/semiconductor structure, we have designed a novel DFB laser with an addressable-period, location-dependent chirped-grating which can be precisely controlled and conveniently applied for wavelength tuning. In contrast to thermal tuning mechanisms, the tuning rate is limited only by the laser cavity dynamics. Previous work demonstrated a tunable DFB laser with a similar tuning mechanism [23, 24], but with insufficient feedback from the grating patterned on the device, the laser operated only with the pump stripe oriented normal to the laser facets, introducing Fabry-Perot (F-P) feedback and associated mode-hops and discontinuous tuning. That laser achieved a quasi-continuous tuning range of 65 nm centered at 3.2 μm , with output wavelength hopping between different F-P modes and only operated at low pump power. Attempts to improve the DFB operation with a higher coupling strength were not successful; numerous mode hops were observed, although these were not associated with F-P effects and their origin was initially unclear. In this contribution, we show that these mode hops were due to the chirp along the lasing stripe (longitudinal chirp) inherent in the optical scheme we used to form the grating. In this paper, we demonstrate an improved optical configuration to pattern the chirped grating for wavelength tuning that leads to a reduced longitudinal chirp, and the fabricated laser device achieves stable, high-power DFB lasing as well as continuous tuning with successful F-P mode

suppression and an 80-nm wide wavelength tuning range centered at 3.1 μm .

Details of the fabrication and characterization of the device are given in appendix A, a manuscript that has been submitted for publication to the Journal of Quantum Electronics.

Deterministic nanowire fabrication for next generation electronics

Electron transport in low dimensional structures is both of fundamental scientific interest and increasingly relevant to future advances in electronics. One-dimensional (1D) transport has been investigated with inherent 1D organic chains such as TTF-TCNQ,^{25,26} carbon nanotubes,²⁷ electron channels fabricated by dry etching or squeezed by a split gate in a FET,²⁸ free-standing semiconductor NWs grown by laser ablation or vapor-liquid-solid (VLS) chemical reactions,²⁹ and metal quantum point contacts formed by connecting two metal electrodes in a scanning tunneling microscope.³⁰

Semiconductor nanowires (NWs) along with carbon nanotubes and graphene have been identified as important directions for future electronics as the limits to traditional scaling of Si integrated circuits become more imminent.^{31-32,33} NW research is still at an early stage, most efforts are concentrated on NW fabrication and limited one-by-one assembly.⁹

VLS growth has both a variation of nanowire sizes, as a result of the varying sizes of the metal seeds used to initiate the growth, and a random placement again as a result of the variation in seed positions.³⁴ For most VLS nanowires, the growth is perpendicular to the substrate makes contacting and organizing the nanowires into circuits quite complex.³⁵

There is increasing interest in integrating InAs or related III-V nanowire materials as the conduction channel in future generations of electronics as a consequence of the high mobility of these materials as compared with silicon.³⁶ Current ICs have upwards of several billion transistors with transverse dimensions today as small as 15 nm, and spaced by ~ 15- to 20-nm, so integration of III-V materials using any sort of post growth processing is problematic - the nanowires have to be grown in place. The lattice mismatch between Si and InAs precludes a simple epitaxial solution without a very thick buffer layer, which is not feasible within the current IC scaling paradigm.

It is clear that lithographically defined positioning and control of the nanowire size would be a preferable approach. Previously, we have shown the growth of GaAs nanowires horizontally on a GaAs surface.³⁷ This required a lattice-matched material system such as AlGaAs and was not applicable to technologically important systems such as InAs on Si. The process also required a sacrificial layer such as AlGaAs that could be oxidized after growth to isolate the nanowire from the substrate, introducing additional strain as a result of the oxidation.

Many groups have reported the growth of InAs nanowires vertically from a Si(111) surface.³⁸⁻³⁹ However, this has many of the same issues as the VLS growth in terms of making large numbers of 3-terminal transistor devices in a well defined circuit. The Si(111) surface is not suitable for electronic integration which is uniquely available on the Si(001) surface as a result of the properties of the SiO₂/Si(001) interface.

In homo- and hetero-epitaxy on a (001)-oriented Si substrate, nanowires (NWs) grow in $\langle 111 \rangle$ directions that are 35.3° -off from the substrate surface. This causes two major problems in their application to Si and III-V microelectronics; one is the random growth along eight available $\langle 111 \rangle$ directions on (001) and the other is the fabrication of contact on the NWs. This invention resolves the first issue by employing a pillar or a post structure on (001) and locating the openings for NW nucleation at the side of the pillar (side hole opening) to induce a single (111)-orientation facet out of eight available $\langle 111 \rangle$ directions so that the opening and the resulting facet at the top of the pillar guide an NW to grow a predetermined single direction. Also, this invention provides a solution for the other issue by bending an NW toward a nearby step so that its upper part physically touches the step surface parallel to (001) for coplanar contacts and further processing.

Figure 1 shows the process of forming the side hole opening. The process can be summarized as follows:

Step 1 Fabricate a pillar on a Si(001) substrate [Fig. 1(a)].

Step 2 Passivate the surface with an SiO_2 film by thermal oxidation [Fig. 1(b)].

Step 3 Cover the surface with a photoresist (PR) film with a thickness greater than the pillar height for planarization and isotropically etch the PR film from the top with an oxygen plasma to expose the upper part of the pillar [Fig. 1(c)].

Step 4 Cover the surface with double deposition of Cr film by e-beam evaporation [Fig. 1(d)]. To keep a Cr film-free area at one side of the pillar that is aligned to (110) plane of the Si substrate by the shadow mask effects from the pillar, the angle between the Cr-beam fluxes (α) in top-down view and their incident angle (β) in cross-sectional view of Fig. 1(d) must be properly adjusted. In this process, $\alpha < 45^\circ$ and $\beta > 45^\circ$ work for this purpose. The Cr-free area bounded by the PR film and the Cr film corresponds to the area for a side hole opening.

Step 5 Remove the SiO_2 film exposed through the side hole opening by dry etching [Fig. 1(e)].

Step 6 Fabricate a single (111) facet by anisotropic wet etching based on KOH through the side hole opening [Fig. 1(f)].

Step 7 Remove the PR film and the Cr film [Fig. 1(g)].

Figure 1(h) shows top-down view scanning electron microscopy (SEM) images of an SiO_2 -passivated pillar with a side hole opening at the right side (top) that corresponds to the top of Fig. 1(g) and an InAs NW grown from it (bottom).

Typical NW epitaxy using VLS or a pattern with a mask film is achieved on a planar (111) plane in vertical direction. Such growth is realized on a (001) plane with an angle from the substrate by 35.3° . This is possible by fabricating a nanoscale (111) facet small enough for growth of a single NW into a Si(001) surface by the process explained in Fig. 1. In Fig. 2, a pillar structure shown in Fig. 1(g) is illustrated with a nearby Si step. In this invention, as mentioned earlier, an opening

in the SiO_2 film is fabricated at the side of the pillar and the (111) facet prepared at the top guides the growth of NW in a single direction. As shown Figs. 1(h) and 3, an NW array grows vertically from the (111) facet resulting in 35.3° -tilt from the Si(001) substrate. After growth, the NW in Fig. 2 (or each NW in Fig. 3) is elastically bent toward the nearby step to make it parallel to Si(001) and to physically contact the step surface. Figures 4 and 5 show some examples of InAs NW bending. These bends were mechanically performed by a metallic needle for the demonstration of elastic bending of InAs NWs grown on Si(001) substrate. The length and diameter of the NW in these figures are $\sim 4 \mu\text{m}$ and $\sim 100 \text{ nm}$, respectively. Basically, NW bending is available by electric force and surface tension or cohesive force of a liquid, as reported. Figure 6 shows such examples. Importantly, Figure 5 reveals the elastic bending of InAs NWs with the bending angle up to $\sim 50^\circ$ that is enough for the process in Fig. 2.

After bending with a physical contact to the step surface, an NW can be freed from the root (or from a Si pillar) by cutting the lower part which contains a lot of defects. The process of this invention therefore can grow and locate many NWs at lithographically determined positions on a Si(001) surface. Once the bending is completed, the standard process for planar devices can be applied to the NW. This invention is highly favorable for large lattice-mismatched NW heteroepitaxy on (001) since the small physical contact area of the NW to the substrate induces a minimal stress.

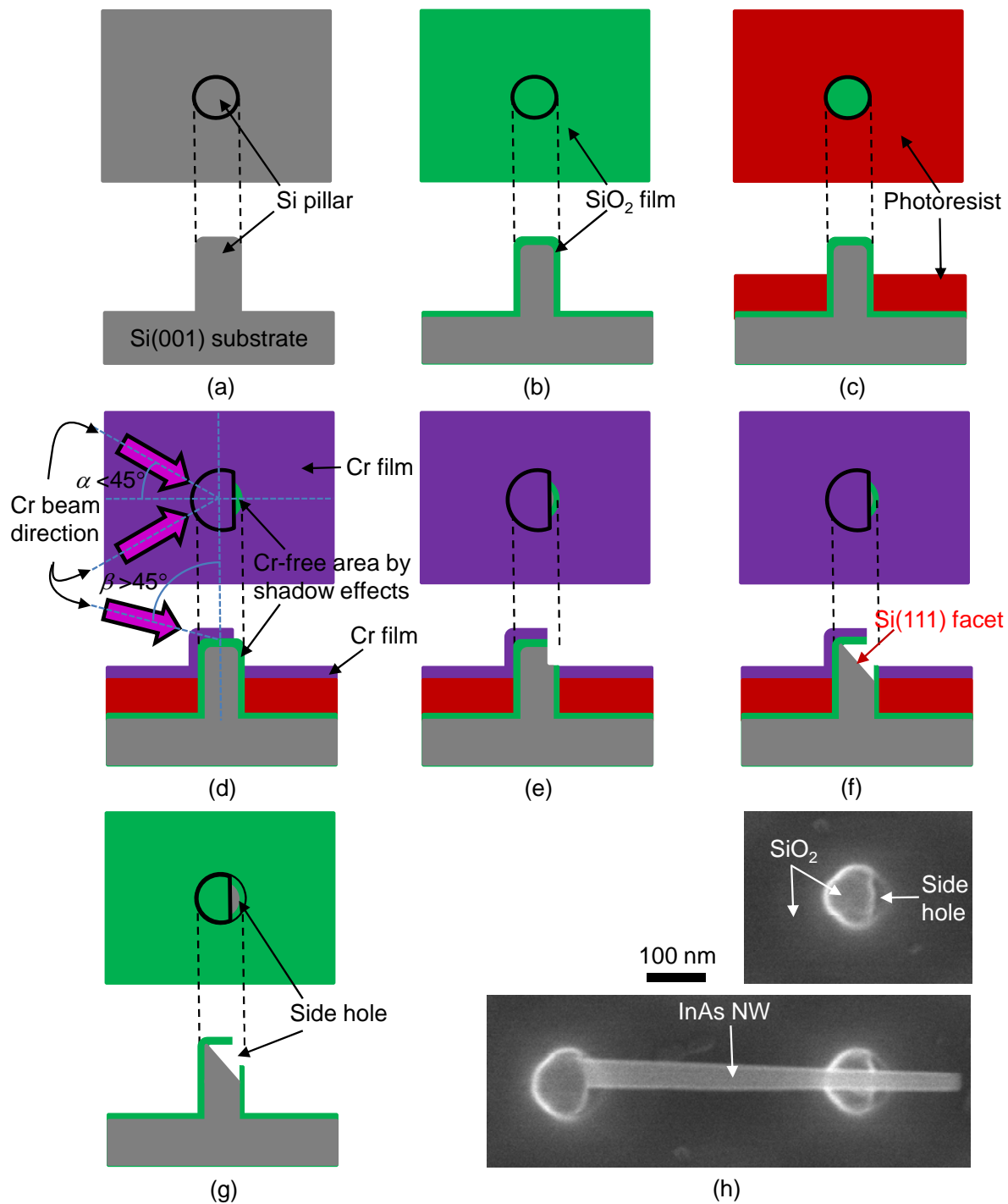


Fig. 1 (a) – (g) A schematic process flow of the side hole opening for InAs NW selective epitaxy. The top and bottom of each figure correspond to a top-down and a cross-sectional view. (h) top-down SEM images of a pillar corresponding to the top-down view of (g) (top) and an InAs NW grown from the side hole opening (bottom).

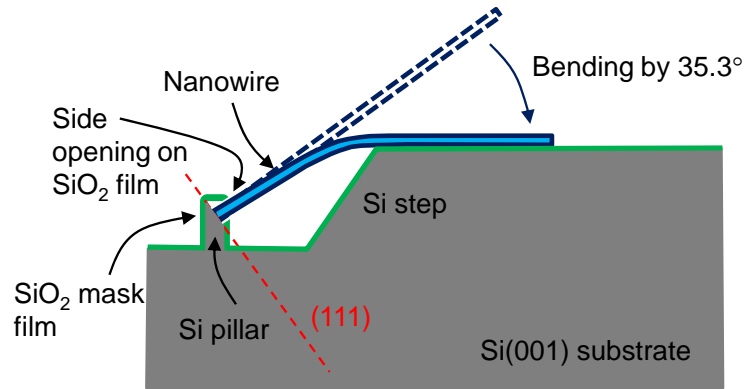


Fig. 2 A schematic illustration of selective growth of an NW on a Si(001) substrate with a pillar structure passivated by SiO₂ film, as shown in Fig. 1(g). A dashed and a solid blue NW correspond to an NW before and after bending, respectively.

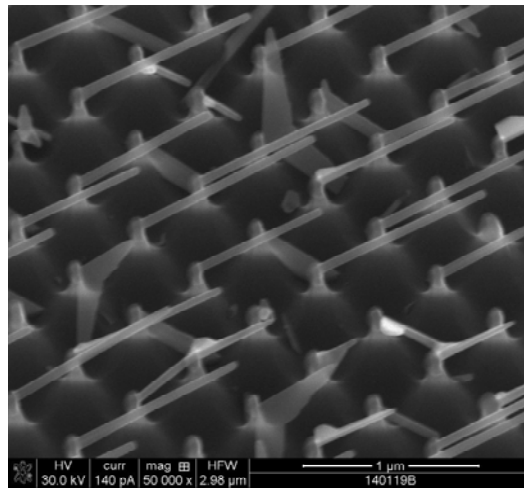


Fig. 3 An SEM image of an array of InAs NWs grown on a Si(001) substrate with the procedure for Fig. 1. Most of them are aligned to a single direction. All NWs are as-grown without bending, corresponding to the dashed NW in Fig. 1. The period of and length of the NWs are 500 nm and ~800 nm, respectively.

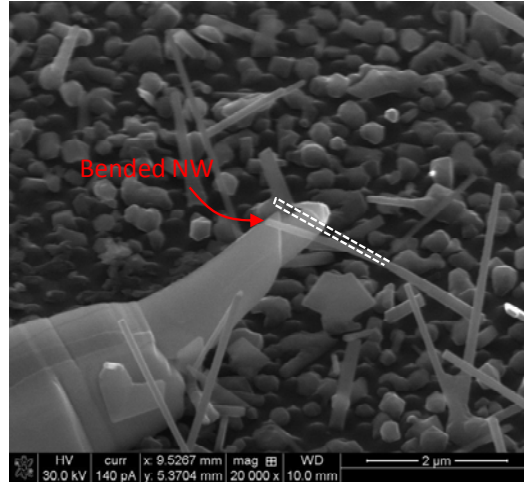


Fig. 4 A minor bending of an InAs NW by a metallic needle. A dashed line denotes the original position of the NW before bending.

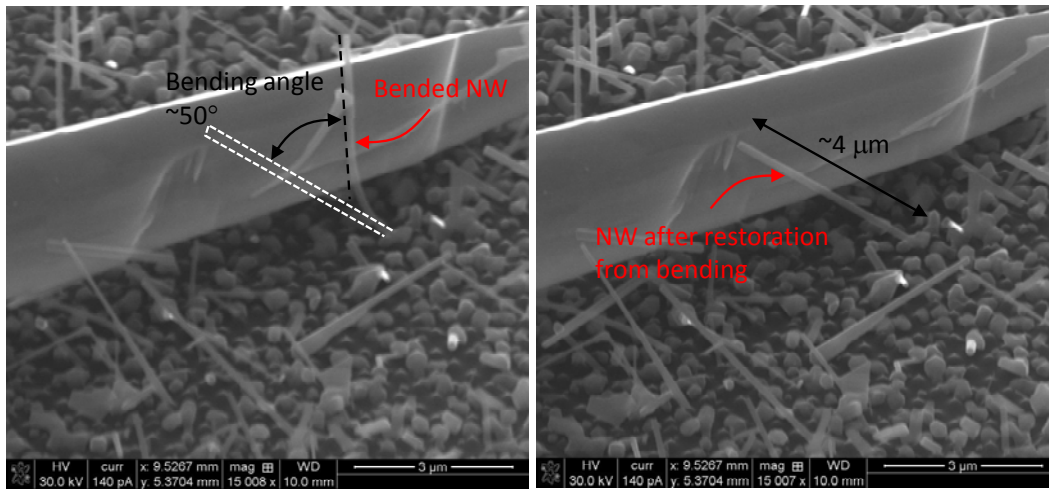


Fig. 5 A major bending of an InAs NW by a metallic needle (left) and its restoration from bending (right). A dashed line in the left denotes the position of the NW after restoration which is exactly the same location as that before bending, implying elastic recovery.

Planar gate-all-around complementary tunnel field effect transistors by dual nanowires epitaxially grown on Si(001)

For last several years, fin-based field effect transistors (FinFETs) have been focused on for low power supply voltage, V_{dd} , and subthreshold swing (SS) approaching 60 mV/dec, the theoretical limit on MOSFET (metal-oxide-semiconductor field effect transistor). Recently, Intel has reported Si FinFET with 10nm node technology and, as seen in Fig. 7, IBM and its collaborators have announced commercial 7 nm node FinFETs with SiGe as a channel material. However, this fabrication inherently retains a MOSFET structure in charge transport mechanism that limits its device- to system-level application for the next generation transistor requiring further reduction of V_{dd} and SS below 60 mV/dec. To resolve this issue, tunnel field effect transistors (TFETs) are emerging as potential replacements for Si CMOS transistors in device- and circuit-level architectures.[40] TFET relies on band-to-band tunneling (BTBT) that is totally different from MOSFET in charge transport. It has well-known major advantages that can outperform MOSFET; sharper SS at low V_{dd} , better saturation behavior at high source-to-drain bias, V_{ds} , and smaller Miller capacitance.[40] They lead to lower switching energy, better circuit gain, and less delay time in digital logic. Owing to these characteristics, TFET can be 8× faster than MOSFET at $V_{dd} \sim 0.35$ V that can impact the latest CMOS technology mentioned earlier. Another simulation in Fig. 8 also suggests that it can remarkably reduce power consumption and delay in digital circuits such as flip-flop compared with Si FinFET.⁴¹ Bandgap engineering of heterojunction TFET has demonstrated better performance in analog as well as digital circuits with higher on-state current, I_{on} . The most recent comparison of a 16-nm low-power Si FinFET CMOS with reported TFETs in both experiment and simulation are summarized in a recent review article.⁴² Although several TFETs with different materials and fabrication technologies have been reported, most of them are incompatible with future Si nanoelectronics as a result of degraded material qualities, complicated processing, and/or a substrate orientation incompatible with Si(001).

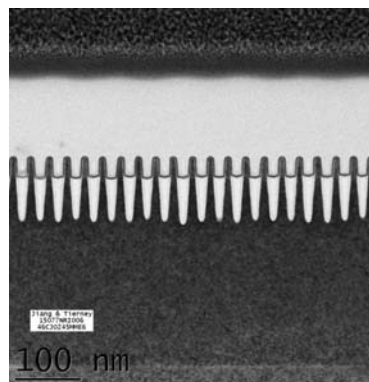


Fig. 7 Bulk 7nm SiGe FinFET with a 30nm pitch (<https://www-03.ibm.com/press/us/en/pressrelease/47301.wss>)

In principle, complementary (C-) TFET devices can be achieved with an identical material by controlling either electrons or holes to tunnel at the reverse biased p - n junction or p - i - n structure with gate bias polarity.⁴³ A few research groups have reported top-down processed, single material C-TFET.^{44,45} Because of different effective masses and mobility

depending on carrier type, however, the highest performances for both p - and n -TFET from the same material that can outperform Si CMOS has yet to be achieved. Except for 2-dimensional materials such as graphene and transition-metal dichalcogenides such as MoS₂, which need further study for industrial applications, In_xGa_{1-x}As and Ge_ySn_{1-y} have been proposed for n - and p -TFET respectively with the best performances demonstrated to date particularly in I_{on} at low V_{dd} , the most critical issue on TFET.^{46,47} They satisfy small direct bandgap and carrier effective mass for high tunneling probability and low resistance channel to increase I_{on} , which are the primary conditions of complementary (C-) TFET to compete with Si CMOS.⁴² However, they were grown separately on InP and Ge substrates, respectively. For the direct compatibility with the established Si technology, they must be accommodated into a single substrate especially a (001)-oriented Si substrate that is the main stream of semiconductor industry in substrate material and orientation.

The TFETs referred above had a conventional FET structure and were fabricated with standard FET processes. Structurally, nanowires (NWs) enabling gate-all-around (GAA) channel control are the best candidate for the next generation transistor. Theoretically, GAA can completely shut off the channel current of an NW, crucial to TFET that requires high I_{on}/I_{off} ratio at low V_{dd} . This work introduces CTFETs implemented with tandem axial p - i - n NWs with different materials individually optimized for the n - and the p -TFET that are epitaxially grown on a single Si(001) substrate by nanoscale patterned growth (NPG) assisted by vapor-liquid-solid (VLS) method.⁴⁸ To our knowledge, any NW TFETs epitaxially grown on Si(001) have not been reported yet. In this work, In_xGa_{1-x}As and Ge_xSn_{1-x} which can be deployed to heterojunction devices for higher I_{on} with a smaller bandgap source or a larger bandgap drain are suggested for n - and p -TFET respectively, as a prototype C-TFET consisting of group III-V and group IV NWs. NPG for this dual material NW epitaxy is achieved on a non-planar Si(001) substrate that is ideally fabricated for the C-TFET by preferential VLS method. Dual material NW epitaxy on a single substrate is guided by two different metal catalysts spatially separated from each other with a nanoscale 2-dimensional (2D) alignment on the substrate surface that induce preferential VLS reaction of individual materials depending on metal species and growth temperatures.

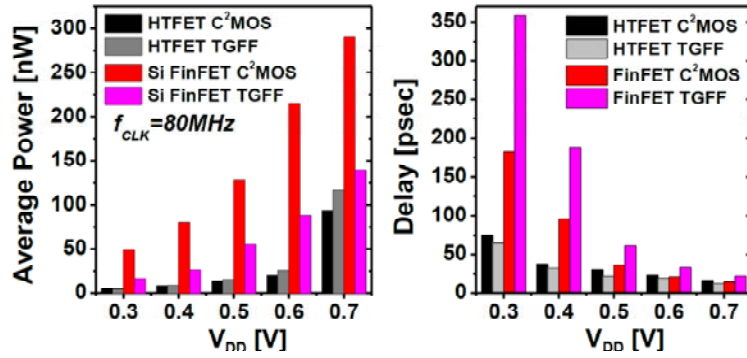


Fig. 8 (a) Average power consumption and (b) delay of C²MOS and double transmission gates (TGs) flip-flops at 0.3-0.7 V [2]

Basically, NPG relieves the lattice mismatch between NW and substrate, and effectively suppress misfit dislocations and their propagation. This allows more degrees of freedom in the material selection of NWs on Si which enhances the feasibility of NW C-TFET. We demonstrated NPG of III-V NWs on a GaAs(001) and a Si(111) substrate ten years ago.^{49,50} Since then, there have been substantial efforts to utilize them for the integration into Si microelectronics. But a couple of critical issues we noticed in our research, (111)-oriented substrate for vertical NWs and their polytypism on this orientation, had persistently hindered its progress. Recently, the latter has been resolved by the variation of growth parameters and NPG of stacking fault-free zincblende GaAs NWs and pure wurzite InGaAs NWs on (111)-oriented substrate have been reported.^{51,52} However, they were still on (111) substrates. In this work, we propose a simple but decisive solution for the former issue with physical NW bending that enables the epitaxial growth of NWs on (001)-orientated substrate and the planar device process for C-TFET with dual NWs by preferential VLS method. This ideally provides seamless compatibility with current Si microelectronics and can potentially outperform the latest Si CMOS.

NWs have been examined in various ways. Among them, epitaxial growth is superior than any other techniques for defectless single crystalline structure, well-defined crystal shape by faceting, reduced surface states and roughness, abrupt heterojunction and doping profile, and direct growth on a substrate. These advantages are very important to the issues of TFET mentioned earlier such as further reduction of I_{off} by the absence of channel thickness variation, sub-60 mV/dec room-temperature SS unscreened by trap-assisted tunneling, and suppression of ambipolar characteristics for high I_{on} .

The C-TFET of this work is based on two innovative ideas, one is epitaxy of dual NWs on a single Si(001) substrate by preferential VLS method and the other is physical NW bending. They are illustrated in Fig. 9. Preferential VLS method proceeds with two different metal catalysts that are individually optimized for NW materials. It applies to a non-planar Si(001)

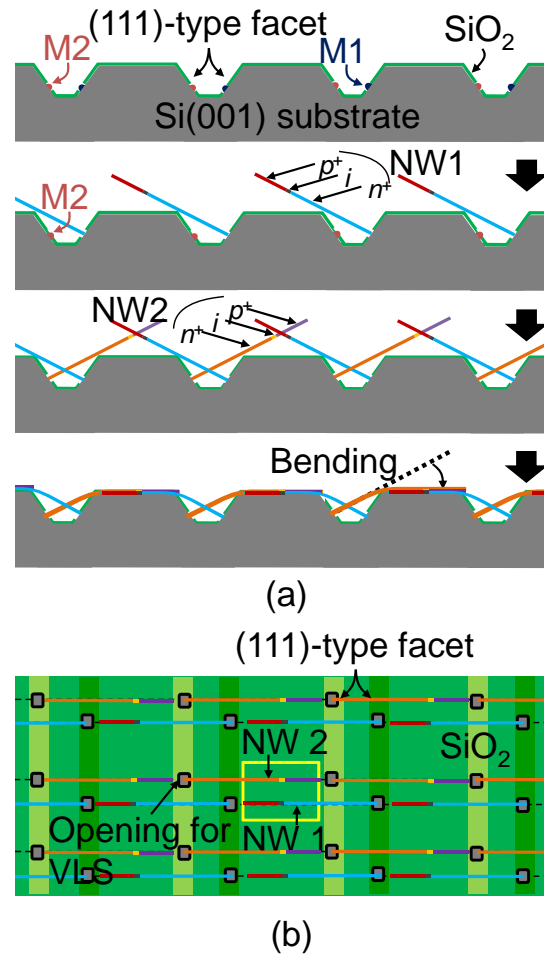


Fig. 9. Schematic illustration of preferential VLS method and physical bending with two different metal catalysts, M1 and M2 for sequential epitaxy of NW1 and NW2. (a) Cross sectional view. The process flows from top to bottom. (b) Top-down view of the bottom of (a) that reveals the paired NWs for CTFET (NW1 and NW2 in a yellow box).

substrate that provides a array of one-dimensional groove pattern consisting of (111)- and (001)-type facets on the surface, followed by off-axis double deposition of metal films leaving metal films separately aligned on facing (111)-type facets in each groove, as shown at the top of Fig. 9(a). Individual metal films are turned into droplets for VLS by thermal treatment. Using different precursors arranged for sequential growth, $\text{In}_x\text{Ga}_{1-x}\text{As}$ and $\text{Ge}_y\text{Sn}_{1-y}$ NWs (NW1 and NW2 in Fig. 9) are grown on (111) facets fabricated on a Si(001) substrate with these metal droplets as VLS catalyst. Based on the database of liquid-solid phase diagram, Au and Sn (M1 and M2 in Fig. 9) are assumed as metal catalysts for $\text{In}_x\text{Ga}_{1-x}\text{As}$ and $\text{Ge}_y\text{Sn}_{1-y}$ respectively. Typical growth temperature of $\text{In}_x\text{Ga}_{1-x}\text{As}$ with Au catalyst is $\sim 500^\circ\text{C}$ while that for $\text{Ge}_y\text{Sn}_{1-y}$ with Sn speculated from the liquid-solid phase diagram of Ge-Sn alloy and the reported data for its epitaxy would be $\sim 160^\circ\text{C}$. Since both Ga-Sn and In-Sn alloys are in liquid state around 500°C regardless of their composition that is far above their eutectic points, no VLS growth happens at the site of Sn droplet and the epitaxy of $\text{In}_x\text{Ga}_{1-x}\text{As}$ proceeds mainly at the site of Au when the precursors for this NW are supplied to a reactor. On the other hand, 160°C is lower than the eutectic points of Ge-Au and Sn-Au alloys. It implies they would be in solid state for all composition during the subsequent growth of $\text{Ge}_y\text{Sn}_{1-y}$ by the precursors for Sn as well as Ge, and Au doesn't play a significant role of a catalyst for it. This assumes the absence of vapor-solid-solid (VSS) process and insignificant vaporization of Sn during growth of $\text{In}_x\text{Ga}_{1-x}\text{As}$ at $\sim 500^\circ\text{C}$. If the vaporization is noticeable, additional amount of Sn to compensate it can be considered in its deposition before epitaxy. In the phase diagram, $\text{Ge}_y\text{Sn}_{1-y}$ only with y very close to 1 would be available as a solid alloy in this VLS and the precursor for Sn may need for smaller $y \sim 0.92$ to achieve direct bandgap required for high tunneling probability in TFET. This is the basic principle of preferential VLS method for dual NWs on a single substrate.

The metal catalysts proposed here are based on the phase diagrams of individual catalyst metal-NW material mixtures. There could be other optimal combinations with the given materials for NW growth along with the consideration of the vapor pressure of metal catalysts. This is one of the major research topics in this work. The sequential NW epitaxy ordered by decreasing growth temperature would be desirable to avoid the sublimation of the first-grown NWs in the growth of the second NWs. If their preferentiality of VLS depending on metal catalyst is sufficiently pronounced at the same growth temperature, the sequential growth in Figs. 9(a) can be replaced by a simultaneous single epitaxy. Eventually, different metal catalysts for dual material NW epitaxy on a single substrate by preferential VLS method is highly advantageous in case where the location of two NWs must be spatially separated from each other for their different physical/chemical properties and device processing/performance.

After completing dual NW by epitaxy, physical bending is applied to lay them on a nearby Si(001) facet passivated with an SiO_2 film, as shown at the bottom of Fig. 9(a). This is another important idea of this work. Nanoimprinting can be employed for this purpose. The maximum bending angle at any spot along the NWs does not exceed 35.7° , as indicated in Fig. 9(a). NW bending has been investigated for the physics related to the elastic properties and its application

to flexible substrates.⁵³⁻⁵⁵ Several reports have demonstrated the physical bending of NWs before fracture that is sufficient for this work. By this bending, the NWs can be treated as in-plane NWs on Si(001).

In this work, therefore, two different NWs are epitaxially grown on (111) facets in the opposite directions in a single groove fabricated on a Si(001) substrate by VLS method, and undergo physical bending for a planar device process that leads to horizontally disposed NWs on a Si(001) surface directly compatible with conventional CMOS technology. In other words, NW1 and NW2 in Fig. 3 grow on a Si(001) substrate along $\langle 111 \rangle$ but are forced to lie on the substrate for planar device processing by postgrowth bending. The $\langle 111 \rangle$ direction is the optimal direction for NW fabrication, but is not CMOS compatible. The bending process provides a simple technique both to grow the nanowires along $\langle 111 \rangle$ and to fabricate transistors in a planar process on a Si(001) substrate. This process combines the advantages of thickness control and doping profile available to vertical NWs on (111) but also enables the application of established planar CMOS processing on (001) by physical bending.

The sequential growth of NWs relies on their different reaction (or growth) rates at given metal catalysts. Cross wetting between them would be another issue on it. If the growth rate difference is not significant, certain growth of NW1 at the site of M2 would be inevitable during growth of NW1 at the site of M1 and vice versa in Fig. 9. But this does not disturb the practical device structures in individual NWs seriously since the former (NW1 grown at the site of M2 before growth of NW2) would be located at the root of NW2 and the latter (NW2 grown at the site of M1 after growth of NW1) is near the tip of NW1, which could be easily excluded from the actual device region during device processes after bending. This insensitivity provides additional degrees of freedom in choosing metal catalysts. The top-down view illustration at the bottom of Fig. 9(b) reveals a 2D array of paired NWs. In this figure, a pair of NWs oppositely grown from (111) facets form a semiconductor-on-insulator (SOI) structure on an SiO₂ film of a Si(001) substrate.

Figure 10 is a GAA C-TFET inverter, as an example of a logic circuit, fabricated with two adjacent NW TFETs in the yellow box indicated at Fig. 3(b) with drain underlap. The dimension of NWs for C-TFET targeted at the early stage of this work would be sub- μm in length

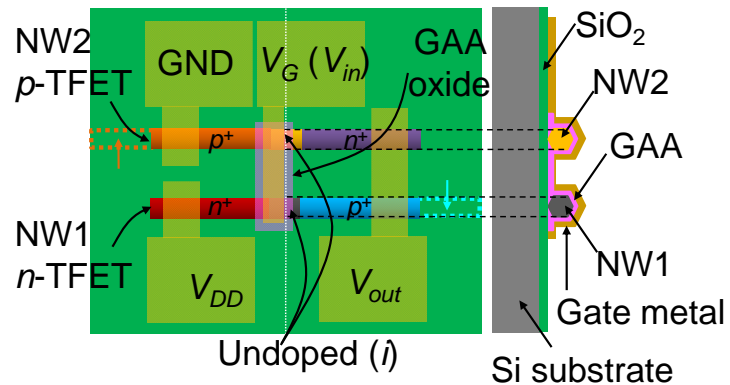


Fig. 10 An inverter designed with a pair of drain-underlap NW TFETs in a yellow box in Fig. 3(b) with top-down view (left) and cross-sectional view along the white dotted line on the left (right). The two bold dashed rectangles with arrows on the left mean the root sections of NWs purposely removed for their electrical/mechanical isolation from the substrate after bending.

and less than 30 nm in diameter. At this dimension and the range below it we pursue later, VLS allows a non-tapered, tandem axially doped NW with a well-defined single (111) facet at the NW/metal droplet interface at the end during epitaxy that is perpendicular to the NW growth direction. The (111) facet is crucially important to provide an abrupt doping profile across a ~10 nm-thick, undoped *i*-region between p^+ and n^+ regions for source and drain. Doping must be individually controlled so that BTBT is available from one heavily doped region to the other through the *i*-region controlled by the gate voltage in each NW. The strain induced by the bending is strongest over the grooves but can be reduced or eliminated by etching out the root section of the NWs indicated with dashed lines in Fig. 4, after bending.

Generally, processing temperatures of Si and III-V considerably different from each other have been regarded as another difficulty in their integration on a single substrate. The Ge-Sn alloy employed in this work can be processed at the temperatures not very different from those of InGaAs ternary alloy. Furthermore, high *K* dielectrics developed for Si and III-V can be directly applicable to the NWs of this work. These enhance the feasibility of group IV and III-V NW C-TFET on a single Si substrate. If the NWs require different temperatures for gate dielectric and ohmic metal, a sequential process for them ordered by the decreasing process temperatures (i.e., photography for selective deposition of the gate oxide and ohmic metal, and the annealing for NW2 first and those for NW1 later if NW2 requires higher annealing temperature than NW1 for ohmic contact, to reduce the thermal budget on the ohmic metal of NW1) would be available in planar processing.

Scientific and Technological Impact

Semiconductor NWs form a new frontier that can provide the ultimate solution for future semiconductor nanoelectronics. The goal of this work is to achieve dual material GAA NW C-TFET operating at V_{dd} under 0.5V with SS of sub-60 mV/dec and I_{on} competing with Si FinFET on a Si(001) substrate. There are, however, a lot of issues that must be investigated for this practical applications. Dual NW epitaxy suggested in this work that relies on preferential VLS method has strong potential for multiple hetero-integrations into Si microelectronics. It requires intensive study for the most optimal pairing of catalysts and NW materials. Sn-alloyed group IV materials employed in this work is highly promising in optoelectronics as well as TFET but have been rarely investigated particularly with Sn as a metal catalyst.⁵⁶ Also, axial heterostructured NWs with in-situ doping are extremely critical to the heterojunction devices but still at the initial stage in epitaxy. Control of axial and radial growth in VLS process is another important issue. Basically, VLS method and other processes related to it such as VSS or oxide-assisted VLS are not completely understood yet. The electronic band structure and carrier effective mass of NWs must be affected by their nanoscale dimensions and strain associated with it. The physical NW bending proposed in this work is simple and evident in process but also a significant factor to these physical properties. This work will impact these fundamental issues with scientific and technological approaches. Furthermore, NW C-TFET in Fig. 10 resolves several problematic

issues on current CMOS technology and also proposes a new frontline of scientific research as follows:

1. This is planar on Si(001) and therefore directly accommodated into mature CMOS technology with negligible current leakage by GAA on SOI with more than 10^{10} devices/cm² integration.
2. C-TFET can be ideally designed with two different NWs individually for *p*- and *n*-TFET implemented on a single Si(001) substrate, providing an significantly improved performance for both complementary devices that can compete with conventional Si-CMOS.
3. C-TFETs in this work are free from the degradation by the lattice mismatch to Si since the actual NW part used for device is far away from the NW/Si interface. By removing the root region of each NW after bending, the device is completely isolated from the substrate.
4. The *i*-region under the gate is epitaxially grown with a precise thickness control along <111> before bending, like a vertical NW. Such structural advantage provides highly predictable device characteristics with well-defined doping profiles. By sequential VLS growth, the doping level of each NW can be individually controlled to optimize the device characteristics for different applications.
5. This approach dramatically simplifies the GAA process that is extremely complicated in vertical NW FETs especially for C-TFET and also the metallization as a single-level process. Also, it removes any issues related to top-down process for NW TFETs such as surface and interface defects and electronic traps.

Finally, these binary alloy homojunction TFETs can be easily extended to heterostructure or quantum well TFETs such as In_xGa_{1-x}As/ InAs and Ge_xSn_{1-x}/Ge for better device performance. Also, III-V, II-VI, and other group IV materials are available for heterostructured NWs for not only improved tunneling characteristics of TFET but also other electronic and optoelectronic NW devices. Ultimately, it radically improves process reliability and production yield as well as device characteristics, and must be a strong candidate to replace Si CMOS for next generation semiconductor nanoelectronics.

References

- [1] C. Gmachl, R. Kohler, F. Capasso, A. Tredicucci, A. L. Hutchinson, D. L. Sivco, J. N. Baillargeon and A. Y. Cho, "Single-mode, tunable quantum cascade distributed feedback (QC-DFB) lasers between 4.6 and 10 μm wavelength," in *CLEO 2000, volume CWF1*, page 264, 2000.
- [2] C. J. Chang-Hasnain, "Tunable VCSEL," *IEEE J. Select. Topics Quantum Electron.*, vol. 6, no. 6, pp. 978-987, Nov. 2000.
- [3] S. Suchalkin, M. Kisin, S. Luryi, G. Belenky, F. Towner, J. D. Bruno, C. Monroy and R. L. Tober, "Wavelength tuning of interband cascade lasers based on Stark effect," *Future Trends in Microelectronics*, John Wiley & Sons, Inc., 2007, pp. 369-379.
- [4] S. Suchalkin, M. V. Kisin, S. Luryi, G. Belenky, F. Towner, J. D. Bruno and R. Tober, "High-Speed Stark Wavelength Tuning of MidIR Interband Cascade Lasers," *Photonics Technology Letters, IEEE*, vol. 19, no. 6, pp. 360-362, 2007.
- [5] Y. Jiang, L. Li, Z. Tian, H. Ye, L. Zhao, R. Q. Yang, T. D. Mishima, M. B. Santos, M. B. Johnson and K. Mansour, "Electrically widely tunable interband cascade Lasers," *Journal of Applied Physics*, vol. 115, p. 113101, 2014.
- [6] M. Ito and T. Kimura, "Oscillation properties of AlGaAs DH lasers with an external grating," *IEEE Journal of Quantum Electronics*, vol. 16, pp. 69-77, 1980.
- [7] B. Glance, C. A. Burrus and L. W. Stulz, "Fast frequency-tunable external cavity laser," *Electron. Lett.*, vol. 23, pp. 98-100, 1987.
- [8] R. Maulini, A. Mohan, M. Giovannini, J. Faist and E. Gini, "External cavity quantum-cascade laser tunable from 8.2 μm to 10.4 μm using a gain element with a heterogeneous cascade," *Appl. Phys. Lett.*, vol. 88, p. 201113, 2006.
- [9] G. Wysocki, R. Lewicki, R. F. Curl, F. K. Tittel, L. Diehl, F. Capasso, M. Troccoli, G. Hofler, D. Bour, S. Corzine, R. Maulini, M. Giovannini and J. Faist, "Widely tunable mode-hop free external cavity quantum cascade lasers for high resolution spectroscopy and chemical sensing," *Applied Physics B*, vol. 92, no. 3, pp. 305-311, 2008.
- [10] A. Hugi, R. Terazzi, Y. Bonetti, A. Wittmann, M. Fischer, M. Beck, J. Faist and E. Gini, "External cavity quantum cascade laser tunable from 7.6 μm to 11.4 μm ," *Appl. Phys. Lett.*, vol. 95, p. 061103, 2009.
- [11] V. Jayaraman, A. Mathur, L. A. Coldren and P. D. Dapkus, "Very wide tuning range in sampled grating DBR laser," in *13th IEEE Laser Conf. '92*, 1992.
- [12] V. Jayaraman, D. A. Cohen and L. A. Coldren, "Extended tuning range in a distributed feedback InGaAsP laser with sampled gratings," in *OFC'92*, 1992.
- [13] S. Kim, Y. Chung, S.-H. Oh and M.-H. Park, "Design and analysis of widely tunable sampled grating DFB laser diode integrated with sampled grating distributed Bragg reflector," *IEEE Photon. Technol. Lett.*, vol. 16, no. 1, pp. 15-17, 2004.
- [14] B. Mason, G. Fish, S. DenBaars and L. Coldren, "Ridge waveguide sampled grating DBR lasers with 22-nm quasi-continuous tuning range," *IEEE Photonics Technology Letters*, vol. 10, no. 9, pp. 1211-1213, 1998.
- [15] Y. Tohmori, Y. Yoshikuni, H. Ishii, F. Kano, T. Tamamura, Y. Kondo and M. Yamamoto, "Broad-Range Wavelength-Tunable Superstructure Grating (SSG) DBR Lasers," *IEEE Journal of Quantum Electronics*, vol. 29, no. 6, pp. 1817-1823, 1993.
- [16] Y. Tohmori, F. Kano, H. Ishii, Y. Yoshikuni and Y. Kondo, "Wide tuning with narrow line width in DFB lasers with superstructure grating (SSG)," *Electron. Lett.*, vol. 29, pp. 1350-1352, 1993.
- [17] H. P. Gauggel, H. Artmann, C. Geng, F. Scholz and H. Schweizer, "Wide-range tunability of GaInP-AlGaInP DFB lasers with superstructure gratings," *IEEE Photon. Technol. Lett.*, vol. 9, pp. 14-16, 1997.
- [18] I. A. Avrutsky, D. S. Ellis, A. Tager, H. Anis and J. M. Xu, "Design of widely tunable semiconductor lasers and concept of binary superimposed gratings (BSG's)," *IEEE J. Quantum Electron.*, vol. 34, pp. 729-741, 1998.

- [19] B. G. Lee, M. A. Belkin, R. Audet, J. MacArthur, L. Diehl, C. Pflügl, F. Capasso, D. C. Oakley, D. Chapman, A. Napoleone, D. Bour, S. Corzine, G. Höfler and J. Faist, "Widely tunable single-mode quantum cascade laser source for mid-infrared spectroscopy," *Appl. Phys. Lett.*, vol. 91, p. 231101, 2007.
- [20] B. Pezeshki, E. Vail, J. Kubicky, G. Yoffe, S. Zou, J. Heanue, P. Epp, S. Rishton, D. Ton, B. Faraji, M. Emanuel, X. Hong, M. Sherback, V. Agrawal, C. Chipman and T. Razazan, "20-mW widely tunable laser module using DFB array and MEMS selection," *Photon. Technol. Lett.*, vol. 14, no. 10, pp. 1457-1459, 2002.
- [21] Y.-D. Chung, J.-S. Sim, S.-B. Kim, J. Kim, and S.-W. Ryu "Wavelength-selectable 8-channel WDM optical transmitter," *JKPS*, vol. 45, no. 3, pp. 605-608, 2004.
- [22] S. Bao, Y. Xi, S. Zhao and X. Li, "Sampled grating DFB laser array by periodic injection blocking," *IEEE J. Selected Topics in Quantum Electron.*, vol. 19, no. 5, pp. 1-8, 2013.
- [23] L. Xue, S. R. J. Brueck and R. Kaspi, "High-power continuous-wave single-longitudinal-mode operation of an optical pumped DFB laser at $\lambda \sim 3.64 \mu\text{m}$," *IEEE Photon. Technol. Lett.*, vol. 20, no. 9, pp. 727-729, 2008.
- [24] L. Xue, S. R. J. Brueck and R. Kaspi, "Widely tunable distributed-feedback lasers with chirped gratings," *Appl. Phys. Lett.*, vol. 94, p. 161102, 2009.
- 25 Anderson *et al.*, *Remarks on giant conductivity in TTF-TCNQ*. *Solid State Comm.*, 13, 595 (1973).
- 26 Z. H. Wang, E. M. Scherr, A. G. MacDiarmid and A. J. Epstein, *Transport and EPR Studies of Polyaniline: A Quasi-One-Dimensional Conductor with Three-Dimensional "Metallic" States*, *Phys. Rev.* B45, 8-15 (1992).
- 27 Mintmire *et al.*, *Are fullerene tubules metallic?*, *Phys. Rev. Lett.* **68**, 631 (1992).
- 28 Thronton *et al.*, *One-dimensional conduction in the 2D electron gas of a GaAs-AlGaAs heterojunction*, *Phys. Rev. Lett.* **56**, 1198 (1986).
- 29 M. Law, J. Goldberger and P. Yang, *Semiconductor Nanowires and Nanotubes*, *Annu. Rev. Mater. Res.* **34**, 83-122 (2004).
- 30 Agraït *et al.*, *Conductance steps and quantization in atomic-size contacts*, *Phys. Rev.* **B47**, 12345 (1993).
- 31 C. Thelander, P. Agarwal, S. Brongersma, J. Eymery, L. F. Feiner, A. Forchel, M. Schiffler, W. Reiss, B. J. Ohlsson, U. Gösele, and L. Samuelson, *Nanowire-based one-dimensional electronics*, *Matls Today* **9**, 28 (2006).
- 32 O. Hayden, R. Agarwal and W. Liu, *Semiconductor Nanowire Devices*, *Nanotoday* **3**, 12 (2008).
- 33 P. Yang, R. Yan and M. Fardy, *Semiconductor Nanowires: What's Next?*, *Nano Lett.* **10**, 1529 (2010).
- 34 V. Schmidt, J. V. Wittemann, S. Senz and U. Gösele, *Silicon Nanowires: A Review on Aspects of their Growth and their Electrical Properties*, *Adv. Matls.* 21, 2681-2702 (2009).
- 35 S. A. Fortuna and X. Li, *Metal-Catalyzed Semiconductor Nanowires: a Review on the Control of Growth Directions*, *Semicond. Sci. Technol.* **25**, 024005 (2010).
- 36 J. A. del Alamo, *Nanometre-scale electronics with III-V compound semiconductors*, *Nature* **479**, 317-323 (2011).
- 37 S.C. Lee, D.L.Huffaker and S.R.J. Brueck, *Faceting of a quasi-two-dimensional GaAs crystal in nanoscale patterned growth*, *Appl. Phys. Lett.* **92**, 023103 (2008).
- 38 T. Martensson, C.P.T. Svensson, B. A. Wacaser, M.W. Larsson, W. Seifert, A. Gustafsson, L.R. Wallenberg and L. Samuelson, *Expitaxial III-V Nanowires on Silicon*, *Nano Lett.* **4**, 1987-1990 (2004).
- 39 K.Tomioka, J. Motohisa, S. Hara and T. Fukui, *Control of InAs Nanowire Growth Directions on Si*, *Nano Lett.* **8**, 3475-3480 (2008).
- 40 U. E. Avci, R. Rios, K. Kuhn, and I. A. Young, "Comparison of Performance, Switching Energy and Process Variations for the TFET and MOSFET in Logic," in *Proc. Symp. VLSI Technology*, Honolulu, HI, p124 (June 14, 2011).
- 41 M. S. Kim, H. Liu, K. Swaminathan, X. Li, S. Datta, V. Narayanan, "Enabling Power-Efficient Designs with III-V Tunnel FETs," in *Proc. Integrated Circuit Symp. Compound Semiconductors*, La Jolla, CA, p1 (Oct. 19, 2014).
- 42 H. Lu and A. Seabaugh, "Tunnel Field-Effect Transistors: State-of-the-Art," *IEEE J. Electron Device Soc.* **2**, 44 (2014).
- 43 A. M. Ionescu & H. Riel, "Tunnel field-effect transistors as energy-efficient electronic switches," *Nature* **479**, 329 (2011).
- 44 R. Rooyackers, A. Vandooren, A.S. Verhulst, A. Walke, K. Devriendt, S. Locorotondo, M. Demand, G. Bryce, R. Loo, A. Hikavy, T. Vandeweyer, C. Huyghebaert, N. Collaert, A. Thean, "A New Complementary Hetero-Junction Vertical Tunnel-FET Integration Scheme," in *Proc. IEDM Tech. Dig.* 13-92 (2013).
- 45 L. Knoll, Q.-T. Zhao, A. Nichau, S. Trelenkamp, S. Richter, A. Schäfer, D. Esseni, L. Selmi, K. K. Bourdelle, and S. Mantl, "Inverters With Strained Si Nanowire Complementary Tunnel Field-Effect Transistors," *IEEE Electron Device Lett.* **34**, 813 (2013).

- 46 G. Dewey, B. Chu-Kung, J. Boardman, J. M. Fastenau, J. Kavalieros, R. Kotlyar, W. K. Liu, D. Lubyshev, M. Metz, N. Mukherjee, P. Oakey, R. Pillarisetty, M. Radosavljevic, H. W. Then, and R. Chau, "Fabrication, characterization, and physics of III-V heterojunction tunneling field effect transistors (H-TFET) for steep sub-threshold swing," in *Proc. IEDM Tech. Dig.*, Washington, DC, pp. 33.6.1–33.6.4 (2011).
- 47 Y. Yang, S. Su, P. Guo, W. Wang, X. Gong, L. Wang, K. L. Low, G. Zhang, C. Xue, B. Cheng, G. Han, and Y.-C. Yeo, "Towards direct band-to-band tunneling in p-channel tunneling field effect transistor (TFET): Technology enablement by Germanium-tin (GeSn)," in *Proc. IEDM Tech. Dig.*, San Francisco, CA, pp. 16.3.1–16.3.4 (2012).
- 48 R. S. Wagner and W. C. Ellis, "Vapor-liquid-solid mechanism of single crystal growth," *Appl. Phys. Lett.* **4**, 89 (1964).
- 49 S. C. Lee, L. R. Dawson, S. R. J. Brueck, and Y.-B. Jiang, "Anisotropy of selective epitaxy in nanoscale-patterned growth: GaAs nanowires selectively grown on a SiO₂-patterned (001) substrate by molecular-beam epitaxy," *J. Appl. Phys.* **98**, 114312 (2005).
- 50 S. C. Lee, L. R. Dawson, S. R. J. Brueck, and Y.-B. Jiang, "GaAs on Si(111)- crystal shape and strain relaxation in nanoscale patterned growth," *Appl. Phys. Lett.* **87**, 023101 (2005).
- 51 H. Huang, X. Ren, X. Ye, J. Guo, Q. Wang, Y. Yang, S. Cai, and Y. Huang, "Growth of Stacking-Faults-Free Zinc Blende GaAs Nanowires on Si Substrate by Using AlGaAs/GaAs Buffer Layers," *Nano Lett.* **10**, 64 (2010).
- 52 A. S Ameruddin , H. A. Fonseka, P. Caroff, J. Wong-Leung, R. LM Op het Veld, J. L. Boland⁴ , M. B. Johnston, H. H. Tan, and C. Jagadish, "In_xGa_{1-x}As nanowires with uniform composition, pure wurtzite crystal phase and taper-free morphology," *Nanotechnology* **26**, 205604 (2015).
- 53 X. Li, X. L. Wei, T. T. Xu, Z. Y. Ning, J. P. Shu, X. Y. Wang, D. Pan, J. H. Zhao, T. Yang, and Q. Chen, "Mechanical properties of individual InAs nanowires studied by tensile tests," *Appl. Phys. Lett.* **104**, 103110 (2014).
- [16] G. Conache, A. Ribayrol, L. E. Fröberg, M. T. Borgström, L. Samuelson, L. Montelius, H. Pettersson, and S. M. Gray, "Bias-controlled friction of InAs nanowires on a silicon nitride layer studied by atomic force microscopy," *Phys. Rev.* **B82**, 035403 (2010).
- 54 R. E. Iyi, M. H. Madsen, G. Safran, Z. Hajnal, I. EndreLuka, G. Fulop, S. Csonka, J. Nygard, and J. Volk, "In-situ mechanical characterization of wurtzite InAs nanowires," *Solid State Comm.* **152**, 1829 (2012).
- 55 G. Conache, A. Ribayrol, L. E. Fröberg, M. T. Borgström, L. Samuelson, L. Montelius, H. Pettersson, and S. M. Gray, "Bias-controlled friction of InAs nanowires on a silicon nitride layer studied by atomic force microscopy," *Phys. Rev.* **B82**, 035403 (2010).
- 56 Y. Ding, P. X. Gao, and Z. L. Wang, "Catalyst-Nanostructure Interfacial Lattice Mismatch in Determining the Shape of VLS Grown Nanowires and Nanobelts: A Case of Sn/ZnO," *J. Am. Chem. Soc.* **126**, 2066 (2004).

Appendix A

Publications and Patents

Publications:

Xiang He, S. Benoit, R. Kaspi and S. R. J. Brueck

Optically-Pumped Continuously-Tunable Mid-IR Distributed-Feedback Semiconductor Laser

Submitted to IEEE Journal of Quantum Electronics

S. Benoit, Xiang He and S. R. J. Brueck

Controlled Chirp Gratings Fabricated by Interferometric Lithography

in preparation

Patent Disclosures:

Two provisional patent applications were filed based on the work on this program

62/160,917 (filed May 13, 2015)

Seung-Chang Lee and S. R. J. Brueck

Nanowire bending for Planar Device Process on (001) Si Substrates

62/214,578 (filed Sept. 4, 2015)

Seung-Chang Lee and S. R. J. Brueck

Planar gate-all-around complementary tunnel field effect transistors by nanowires epitaxially grown on Si(001)

Appendix B:

Paper submitted for publication to the IEEE Journal of Quantum Electronics

Optically-Pumped Continuously-Tunable Mid-IR Distributed-Feedback Semiconductor Laser

Xiang He, S. Benoit, R. Kaspi and S. R. J. Brueck, *Fellow, IEEE*

Abstract—An 80 nm continuous, mode-hop-free, wavelength tuning range centered at 3.1 μm has been demonstrated for a large area, optically pumped mid-infrared type-II semiconductor distributed feedback (DFB) laser with a spectral linewidth of 1.2 nm at $2.5\times$ threshold and 820 mW single-facet output power, suitable for atmospheric pressure molecular spectroscopy and remote sensing. Wavelength tuning of this DFB laser is achieved by translating the optical pump stripe across the device patterned with a hyperbolically-chirped, location-dependent-period grating. The impact of chirp along the gain stripe is clarified and optimized to allow continuous tuning.

Index Terms— Chirped grating, Distributed feedback laser, Infrared tunable semiconductor laser, Molecular spectroscopy, Remote sensing.

I. INTRODUCTION

THE MID-INFRARED 3- to 5- μm atmospheric transmission window is important for remote sensing and spectroscopic applications because it contains many fingerprint molecular rotation-vibrational absorption lines, such as O-H stretch at 2.8 μm ; N-H stretch at ~ 3 μm , C-H stretch at ~ 3.3 μm . Spectroscopic applications typically require a continuous wave (CW), single-longitudinal-mode (SLM) and mode-hop-free, continuously tunable, narrow spectral linewidth, high-power laser source with good beam quality. In this paper, a unique implementation of tunable DFB laser for spectroscopic applications is introduced; this technique is broadly applicable independent of the wavelength range.

Manuscript received xxxxxxxx, xx, 2015; revised yyyyyy, yy 2016; accepted zzzzzz,zz, 2016. Date of publication wwwwww,ww, 2016. Partial support for this work was provided by the Air Force Office of Scientific Research and by the Defense Threat Reduction Agency. (*corresponding author: S. R. J. Brueck*)

Xiang He was with the University of New Mexico, Department of Electrical and Computer Engineering. His current address is: Global Communication Semiconductors, LLC, 23155 Kashiwa Ct., Torrance, CA 90505. (xhe@gcsincorp.com)

S. Benoit was with the University of New Mexico, Center for High Technology Materials. His current address is Department of Mathematics, Colorado State University, Fort Collins, CO 80523 (steve.benoit@colostate.edu).

R. Kaspi is with the Air Force Research Laboratory, Directed Energy Directorate, Kirtland AFB, NM 87106 (ron.kaspi@kirtland.af.mil)

S. R. J. Brueck is with the Center for High Technology Materials and Department of Electric and Computer Engineering, Albuquerque, NM 87106 (sbrueck@chtm.unm.edu)

Color versions of one or more of the figures in this paper are available online at <http://ieeexplore.ieee.org>.

Digital Object Identifier 10.xxxx/QJE.2016.yyyyyy

Various laser wavelength tuning mechanisms have been demonstrated for semiconductor lasers, for different purposes and with different technical approaches. Approaches to wavelength tuning include thermal/operation temperature tuning [1], variable cavity length with cantilever/piezo actuator driven end-mirror in vertical cavity surface emitting lasers (MEMS/VCSEL) [2], quantum Stark effect [3-5] wavelength tuning by varying bias voltage in inter-band cascade semiconductor lasers (ICLs) and others. Of course, one important category of wavelength tuning techniques uses the dispersion property of a diffraction grating to select the lasing wavelength. Well-known forms of tunable semiconductor lasers in this category include external cavity lasers [6-10], grating coupled sampled-reflector (GCSR) lasers, sampled-grating DBR (SGDBR) lasers [11-14], super-structure grating (SSG) DFB lasers [15-18], and selectable DFB laser arrays [19-22]. External cavity lasers usually consist of a linear gain section and an external diffraction grating which pivots around an axis to select different lasing wavelengths. GCSR and SGDBR lasers are very similar in the sense that both tune their output wavelength using a Vernier effect. The monolithic laser cavities of both types of lasers usually have two or more sections patterned with sampled gratings of different periods which possess comb-like reflection spectra (a series of discrete reflection peaks). The refractive indices of these sections are independently adjusted by varying the bias or current which shifts the gratings' reflection combs. The output wavelength of the laser is the coincident wavelength corresponding to overlapped reflection comb teeth of different grating sections. A selectable DFB array is simply a group of individual DFB lasers with different grating periods for different lasing wavelengths fabricated on a single die, which are individually turned on and coupled out through a multi-mode coupler. To have continuous wavelength coverage, the output wavelength of each individual DFB laser is usually tuned through operating temperature variation.

All of these tunable lasers have their advantages and drawbacks for different applications. External cavity lasers are widely used both in research and industry for spectroscopic applications, especially with quantum cascade lasers (QCLs) thanks to their very wide continuous wavelength tunability and narrow spectral linewidth. The main issues with this type of laser are manufacturability and reliability given the requirements of precise alignment of moving micro parts as well

as the challenging antireflection coating to cover a wide tuning range in the gain section. GCSR and SGDBR lasers are monolithic, rugged, and can be conveniently integrated with an amplifier to achieve relatively high output powers. Typically, their wavelength tuning is discontinuous, and the primary application is to wavelength division multiplexing (WDM) in telecommunication applications or optical integrated circuits. These lasers are less suitable for spectroscopic applications where continuous, monotonic tuning is desired. Selectable DFB arrays, combined with QCLs have been demonstrated for spectroscopic applications thanks to their very wide wavelength tuning range. Normally e-beam grating patterning in GCSR/SGDBR and selectable DFB array lasers makes fabrication complicated and yield low. Wavelength tuning is also very complicated in both types of lasers because individual electronic circuitry is required for section bias/current control as well as operating temperature control.

In pursuit of a spectroscopic/remote sensing solution that combines the continuous tuning of an external cavity laser with the ruggedness and compactness of a monolithic grating/semiconductor structure, we have designed a novel DFB laser with an addressable-period, location-dependent chirped-grating which can be precisely controlled and conveniently applied for wavelength tuning. In contrast to thermal tuning mechanisms, the tuning rate is limited only by the laser cavity dynamics. Previous work demonstrated a tunable DFB laser with a similar tuning mechanism [23, 24], but with insufficient feedback from the grating patterned on the device, the laser operated only with the pump stripe oriented normal to the laser facets, introducing Fabry-Perot (F-P) feedback and associated mode-hops and discontinuous tuning. That laser achieved a quasi-continuous tuning range of 65 nm centered at 3.2 μm , with output wavelength hopping between different F-P modes and only operated at low pump power. Attempts to improve the DFB operation with a higher coupling strength were not successful; numerous mode hops were observed, although these were not associated with F-P effects and their origin was initially unclear. In this contribution, we show that these mode hops were due to the chirp along the lasing stripe (longitudinal chirp) inherent in the optical scheme we used to form the grating. In this paper, we demonstrate an improved optical configuration to pattern the chirped grating for wavelength tuning that leads to a reduced longitudinal chirp, and the fabricated laser device achieves stable, high-power DFB lasing as well as continuous tuning with successful F-P mode suppression and an 80-nm wide wavelength tuning range centered at 3.1 μm .

II. DEVICE DESIGN AND FABRICATION

A. Epitaxial structure

The epitaxial structure of this tunable DFB laser device consists of a three-layer slab waveguide grown on a GaSb:Te substrate which also functions as the waveguide bottom cladding. On top of the substrate, a 1.5 μm thick core layer was grown containing 14 sets of evenly spaced type-II InAs/InGaSb/InAs quantum wells (QW) as the gain medium sandwiched between 100 nm thick integrated absorber layers

optimized to fully absorb the thulium fiber pump laser power at 1.9 μm , offering efficient carrier confinement. Atop the core layer, a 1.5 μm thick layer of GaSb was grown as the top cladding. The refractive indices of bottom/top clad and the core layers of this slab are about 3.82 and 3.842, respectively. This is a low index contrast configuration designed for transverse beam quality. The epi-structure of the slab waveguide is shown in Fig 1.

For the given refractive indices and thicknesses of epitaxial layers in the slab waveguide, three major constraints need to be taken into account in the design of the grating for maximum coupling coefficient, assuming square-wave grating teeth and 50% duty cycle as shown in Fig. 1. First, the Bragg wavelength corresponding to the grating period needs to align with the gain spectral peak, centered at 3.06 μm at ~ 80 K for maximum material gain. Second, the top clad thickness and grating depth (combined to determine the mode confinement factor) need to be chosen to provide sufficient mode confinement ($\Gamma \sim 0.3$) in the epitaxial direction to have practical modal gain. Third, with consideration of the modal gain calculated in the second constraint, a grating depth needs to be determined to produce an appropriate coupling strength ($1 \leq \kappa L \leq 3$) for a $L = 2.5$ mm device cavity length. κL is given by:

$$\kappa L = \frac{\Delta n_{\text{eff}}}{\bar{n}_{\text{eff}}} \frac{L}{\Lambda} = \frac{2|n_{\text{eff},R} - n_{\text{eff},G}|}{n_{\text{eff},R} + n_{\text{eff},G}} \frac{L}{\Lambda} \quad (1)$$

where $n_{\text{eff},R}$ and $n_{\text{eff},G}$ are the effective indices of the slab waveguide with a top cladding thickness at the ridge and groove, respectively, Δn_{eff} is the magnitude of the difference between the two modal indices, \bar{n}_{eff} is the average modal index, and Λ is the grating period.

After considering the trade-off between the mode confinement factor and coupling coefficient, we chose to etch the grating 500 nm deep without thinning the 1.5 μm top clad layer, with the grating period chirped from 410- to 420-nm over a 4 mm long, 2.5 mm wide laser chip length. These values were calculated based on a straight grating, but are applicable for the estimation of hyperbolically chirped grating case.

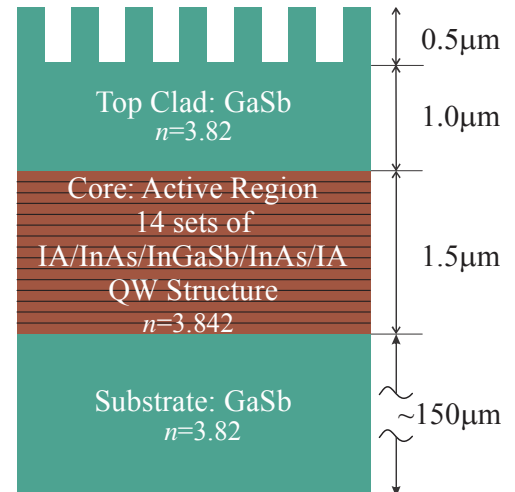


Fig. 1. Schematic of the device structure.

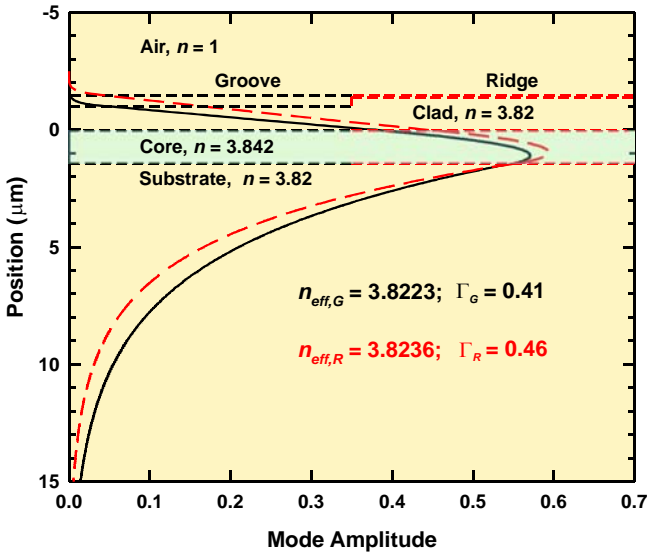


Fig. 2. Calculated mode profiles and effective indices for the groove (black, solid) and the ridge (red, dashed). The gain region between 0 and 1.5 μm is indicated.

In determining the grating dimensional parameters as well as coupling strength and laser mode confinement, an effective index approach was used. The effective refractive indices of the guided mode at the grating ridge and groove were calculated using a 4-layer slab waveguide model with a top clad thickness corresponding to the top clad thickness at the grating ridge (R) and groove (G) segments, respectively. The effective refractive indices as functions of different possible combinations of top clad thicknesses and grating depths were considered to find the optimal grating dimensional parameters. Geometry of this 4 layer slab waveguide is shown in Fig. 2. As an example, the electric field distribution of the TE fundamental mode (the only TE guided mode) in the slab waveguide with both the 1 μm groove cladding thickness (G, black) and the 1.5 mm ridge cladding thickness (R, red). The mode confinement factor, Γ the mode overlap with the gain region, for our device is ~ 0.44 and the coupling strength κL is ~ 2.1 for our 2.5 mm long cavity.

B. Chirped Grating Fabrication

A hyperbolically chirped, location-dependent-period grating for wavelength tuning, a key feature of our DFB laser device, was patterned using interferometric lithography (IL) in photoresist (PR) and then transferred into the top clad of the slab waveguide for wavelength selection and tuning using CI-based inductively-coupled plasma etching. This hyperbolically chirped grating was generated by interference between two spherical wave fronts, using a 355 nm 3rd harmonic Nd:YAG laser as the coherent light source. As shown in Fig. 3(a), the IL experimental setup for the hyperbolically chirped grating is a Lloyd's mirror with an additional plano-convex lens (facing the -Z direction with its back/flat surface in X-Y plane, and lens optical axis co-linear with Z axis) mounted perpendicular to the mirror (in X-Z plane). This lens converts the incident collimated wave into spherical waves before interference. For clarity, two separate beams as shown, experimentally only a single large beam was used.

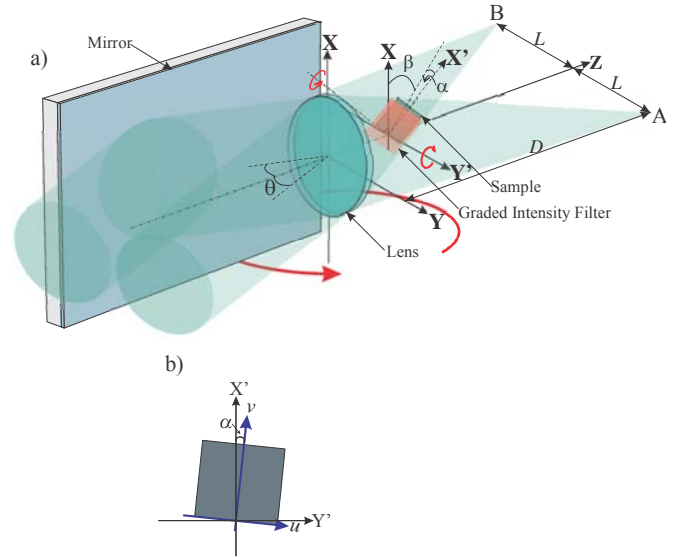


Fig. 3. (a) Interferometric lithography (IL) experimental arrangement for hyperbolically chirped grating pattern. A lens is added to a conventional Lloyd's mirror arrangement to produce the chirped grating. The sample is tilted (β) relative to the optical axis to control the longitudinal chirp along the grating. (b) Sample detail showing the tilt (α) of the grating pattern relative to the cleaved edges of the sample.

This IL approach to generating a chirped grating with interfering spherical waves inherently generates hyperbolic chirps in the grating, characterized by both an approximately linear lateral chirp (along X' parallel to the grating lines) and a quadratic longitudinal chirp (along Y' perpendicular to the grating lines). An important parameter of the grating structure is the ratio of the lateral chirp to the longitudinal chirp. The laser will be optically pumped in a stripe geometry with the long axis of the stripe along the Y' -direction (Fig. 3(b)). The chirp along X' provides the tuning mechanism as the pump stripe is translated; the longitudinal chirp along Y' restricts the active length of the device for a severe enough chirp and can lead to mode-hopping during tuning as discussed below. There are three parameters that describe the impact of the chirp on the tuning of the laser. The first is the lateral chirp $\Delta\Lambda_{lateral}$ (the chirp along the tuning direction that provides the wavelength tuning; this should be as large as possible). The second is the longitudinal chirp $\Delta\Lambda_{longitudinal}$ in the pump strip direction, and the third is the FWHM of the unchirped DFB stop band. These three parameters give rise to two Figures of Merit (FOM) as shown in Eq. (2).

$$FOM_1 = \frac{\Delta\Lambda_{lateral}}{\Delta\Lambda_{longitudinal}} \Big|_{\text{chip area}} \quad (2)$$

$$FOM_2 = \frac{DFB_{\text{stop-band FWHM}}}{\Delta\Lambda_{longitudinal}}$$

where $\Delta\Lambda$ is the pitch variation in the specified direction across the full chip area and the bandwidth of the DFB is proportional to $(n_{eff,R} - n_{eff,G})/\bar{n}_{eff}$. Note that FOM_1 is over the full area of the chip and relates the tuning range to the chirp along a stripe, while FOM_2 is for an individual pump stripe and varies as the stripe is shifted in the tuning direction.

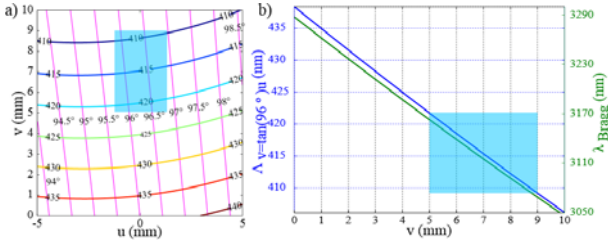


Fig. 4. (a) Grating period and grating line orientation contours as a function of location on the 10x10 die. The blue rectangle is the cleaved device location. (b) Grating period (blue line, left vertical axis) and Bragg wavelength (green line, right vertical axis).

FOM1 is more relevant the overall tuning range of the device, FOM2 to the mode jump behavior and to the effective length of the device that contributes to the lasing.

The optimization goal is to maximize FOM_1 while keeping $FOM_2 > 1$. If the die is tilted relative to the back surface of the lens with an angle β as labeled in Fig. 3(a), a lower $\Delta\Lambda_{\text{longitudinal}}$ value can be obtained than for a die orientation normal to the optical axes. Previous devices were fabricated with the die normal configuration, FOM_2 values for the previous devices were approximately $10\times$ lower than the value for a device fabricated with a tilt angle β of 45° . The improved FOM_2 for the newer $\beta = 45^\circ$ configuration allowed the large mode-hop free tuning range reported in this paper.

For this report two devices were fabricated, one with $\beta = 0^\circ$ and a 75 cm focal length lens (low FOM_2) and one with $\beta = 45^\circ$ and a 37.5 cm focal length lens (high FOM_2). For both samples the other IL parameters were: $\theta \sim 21^\circ$, $\alpha = 6^\circ$ and the $10\times 10 \text{ cm}^2$ laser sample was located 2 mm behind the lens with the center of its bottom edge intersecting the optical axis. Details of the grating fabrication and FOM characterization based on the optical configuration will be presented elsewhere [25]. For high chirp sample the chirp along the lasing stripe was 0.09% ($FOM_1 \sim 12$; $FOM_2 \sim 0.27$) while for the low chirp sample the chirp along the lasing stripe was only 0.007% with a $2\times$ longer tuning range ($FOM_1 \sim 393$; $FOM_2 \sim 3.4$).

The grating pattern and calculated tuning curves for the low chirp device are shown in Fig. 4. As shown in the figure, a 2.5 mm (Y') \times 4 mm (X') final device area was cleaved from the full sample for characterization.

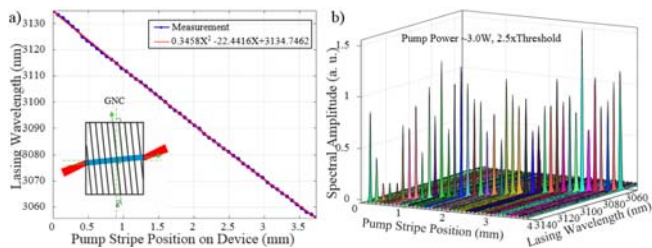


Fig. 5. (a) DFB laser wavelength vs. pump position (u). The experimental data is plotted as discrete points, the red curve is a quadratic fit. The inset shows the grating normal pump configuration (GNC). (b) Waterfall plot of the individual spectra vs. pump position.

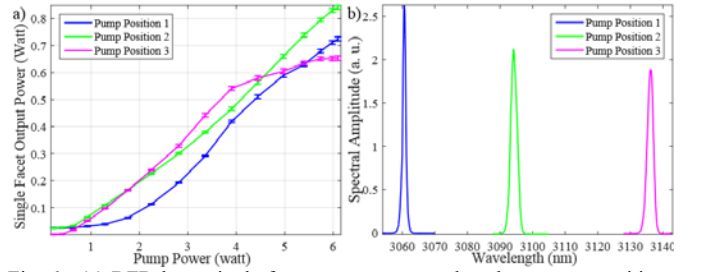


Fig. 6. (a) DFB laser single-facet output measured at three pump positions, with the pump stripe focus adjusted to maximize output power at each position. (b) corresponding device spectra for a pump power of 3.9 W, $\sim 3\times$ threshold.

III. DFB LASER CHARACTERIZATION

A. Optical pump geometry

All of the characterizations of these devices, including the output power, spectral linewidth, and wavelength tuning, were measured for a temperature of $\sim 80 \text{ K}$ in a liquid nitrogen Dewar with optical access for both the pump beam and the output lasing. A thulium fiber pump laser with a CW, 20 W output power at $1.908 \mu\text{m}$ was used. A collimated pump beam with a diameter of $\sim 5 \text{ mm}$ was the excitation source. To ensure uniform pumping across the 2.5 mm wide device, the beam was focused with a cylindrical lens to a pump stripe roughly 70- to 100- μm wide at the device and projected perpendicularly onto the grating-up side of the DFB laser device mounted on the cold finger of the LN2 Dewar. The pump stripe needs to be translated to different locations on the device to select different lasing wavelengths. In practice, the pump beam and device emission collection optics were kept fixed and the LN2 Dewar mounted on a gear-reduced step motor driven translation stage was shifted up or down to vary the pump stripe position on the device. All characterizations were conducted with pump stripe perpendicular to the grating orientation, referred to as grating normal configuration (GNC). Because the grating orientation is tilted 6° relative to the device facets as mentioned, F-P modes due to facet feedback are successfully suppressed. Also because the pump stripe is tilted relative to the device facets, the output beam angle of our DFB laser device is increased to $\sim 23^\circ$ to the facet by refraction at the semiconductor-air boundary, as shown in the inset of Fig 5(a).

B. Wavelength tuning

For device wavelength tuning characterization, the pump stripe position was translated laterally across the whole device width of 4 mm and the spectrum at each pump stripe position was acquired with a monochromator and an InSb photo detector. The low-chirp device wavelength tuning range is shown in Fig 5(a) with the spectral peak wavelength extracted from raw laser output spectra at different pump stripe positions. Fig. 5(b) is the waterfall plot of the spectra. This DFB laser device demonstrated a continuous, mode-hop-free, tuning range of 80 nm, from 3057 to 3137 nm at $\sim 2.5\times$ threshold as labeled.

The single-sided output power of the low-chirp DFB device was measured at many different pump positions, of which three are plotted in Fig 6(a). The output spectra at these three

pump positions at $3.5\times$ threshold are also shown in part b). Thresholds at these different pump positions are not exactly the same, mainly due to fabrication non-uniformities. As seen in the plot, the maximum single facet output power reaches 820 mW, limited by the available pump power, without any sign of saturation except for the stripe nearest the edge of the chip.

The spectral linewidth (FWHM) of the low-chirp DFB laser output at about $2.5\times$ threshold is plotted in Fig. 7(a) across the full tuning range. Typical spectral line width of this device is about 1.2 nm at $2.5\times$ threshold which is adequate for atmospheric pressure broadened spectral investigations, but is too broad for high resolution molecular spectroscopy. As shown in the figure, the spectral linewidth shows a decreasing trend as the pump stripe shifts from one end of the device to the other, suggesting that alignment of the wafer with the pump focal depth plays some role in determining the linewidth, which is most likely due to multiple lateral modes in this many wavelength wide, gain-guided laser cavity. For these initial experiments, there was no adjustment for optimizing pump stripe focusing during the device translation, likely, the actual spectral linewidth of the device will be slightly narrower with an optimized pump geometry configuration.

A very important tuning characteristic for spectroscopy is continuous wavelength tunability without frequency gaps or mode jumps. In traditional unchirped DFB lasers, mode hopping can occur between the two degenerate DFB modes on either side of the stop band. This degeneracy can be lifted by introducing an asymmetry that favors one mode over the other, for example metal grating lines that have more loss for the standing wave mode with intensity maxima at the line positions. In the present case, the longitudinal chirp of the grating provides the asymmetry as discussed below.

To test continuous tuning performance of this low-chirp DFB laser, a high-finesse Fabry-Perot (F-P) interferometer with a fixed cavity length was used. By measuring the transmittance while tuning the output wavelength of the DFB laser, we can characterize both the spectral linewidth and tunability of the device. Slightly shifting the F-P cavity length and rescanning the laser output, allows filling in the spectral measurements to provide a complete tuning curve. As an example for a particular F-P interferometer cavity length of $\sim 365\ \mu\text{m}$, 6 transmittance peaks were obtained as the laser was tuned through the full tuning range as shown in Fig. 7(a), corresponding to the convolution of the six sequential transmis-

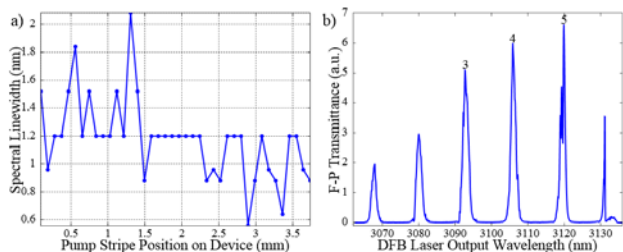


Fig. 7. (a) Spectral linewidth of DFB laser device at different pump positions at pump power of $\sim 2.5\times$ threshold. (b) Fabry-Perot interferometer transmittance measurement with fixed cavity length while tuning DFB laser output wavelength.

sion peaks of the F-P interferometer and the spectra of the tunable DFB laser in the ranges of these 6 peaks. Peak 6 was only partially acquired because the pump stripe was at the extreme end of the laser device. For a $\sim 365\ \mu\text{m}$ F-P cavity length, the free spectral range is $\sim 411\ \text{GHz}$ (13.1 nm); and the interferometer end-mirror reflectance is 0.985 from 3 to 5 μm , giving a finesse of ~ 208 . Each data point in the Fig. 7(a) corresponds to a positional pump stripe translation of $3.15\ \mu\text{m}$, equivalent to a wavelength change of 0.063- to 0.071-nm which is very small compared with the degenerate DFB mode spacing of about 1 nm and the laser F-P mode spacing (with a cavity length of $\sim 2.5\ \text{mm}$) on the order of 0.5 nm. The F-P interferometer resolution under the present condition is close to the wavelength tuning step of 0.063 nm across the whole DFB device tuning range which means all the wavelength tuning steps are resolvable. The spectral line width of our DFB laser, as measured with the interferometer is about 1.3 nm, shown in Fig. 7a), which agrees with the result obtained with the monochromator. Multi-longitudinal-mode operation was not observed in this device. The sub-peaks observable on peaks 3 - 5 are likely due to lateral modes of the laser considering the gain-guided pump stripe width of 70- to 100- μm which can support multiple lateral modes. To check for mode jumps in other regions of the tuning, the F-P interferometer was set to different cavity lengths to interpolate the whole tuning range of the device; mode hopping, corresponding to either the F-P mode space or the degenerate DFB modes, was not observed over multiple measurements.

IV. TRANSFER MATRIX EVALUATION OF WAVELENGTH TUNING

To understand the lasing wavelength and tuning characteristics of our tunable DFB laser, a preliminary model combining the transfer matrix method (TMM) [26-36] with an effective-refractive-indices approach [37, 38], and incorporating the particular geometry of the chirped grating along the laser cavity defined by pump stripe on the DFB device, was developed and implemented. This modeling program was developed as an integrated environment to model: (a) the epitaxial growth structure (for mode analysis and effective refractive indices calculations); (b) the IL pattern generation based on the lens geometry and device position and orientation (for chirped grating solutions); and (c) device performance modules (for pump stripe geometry, cavity TMM construction and threshold lasing wavelength solution). Arguments/results pass among these modules, allowing convenient adaptation to different devices. The principal goal of this model is to predict threshold lasing wavelength as function of pump stripe location on our tunable DFB devices for a given set of parameters, and then to optimize choices of fabrication parameters. Simplifications or assumptions in our model include use of the imaginary part of the refractive index to represent gain/loss of the gain medium, which was taken to vary independently of the real part. The pump stripe width was taken as $100\ \mu\text{m}$ and its power intensity across both its width and length was taken to be constant; the semiconductor gain spectrum was treated as

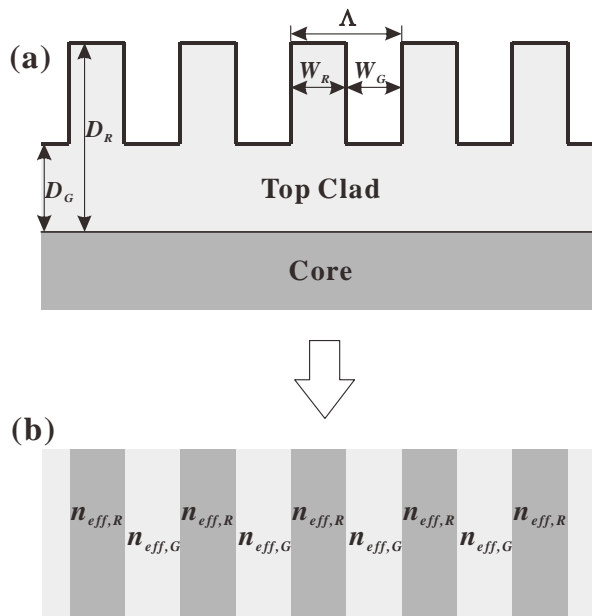


Fig. 8. (a) Chirped grating along the cavity defined by pump stripe on DFB device; (b) Converted layer-stack structure with effective refractive index approach. Layers corresponding to the grating ridge/groove segments.

constant across the whole device wavelength tuning range; and extra losses or leakage of pump power as a result of reflection and scattering from the grating ridges due to non-perpendicularity between pump stripe and the grating lines was ignored.

The approach to determining the threshold lasing wavelength can be summarized as follows. First, the modal indices for the grating groove and ridge (Fig. 2) are determined based on the epitaxial structure. Then the grating periods and line orientations as functions of position along the laser cavity defined by an arbitrary pump stripe projected onto the DFB laser device are calculated based on the IL optical configuration. To gain an initial understanding of the impact of a chirp on the DFB characteristics, a simple quadratic grating profile was used. For comparison with the experimental results in later figures, the grating period variation based on the optical configuration (Fig. 3) was computed. Due to the hyperbolically chirped grating, both grating periods and line orientations vary along the cavity as shown. Along the 2.5 mm longitudinal cavity length of each DFB device, there are ~ 6000 full grating cycles for a 415 nm pitch as well as two fractional periods at the facets due to random cleaving positions which are location-dependent since the grating lines are tilted relative to the facets. These partial periods are important for geometries in which both the cavity F-P and the DFB are aligned, but are ignored in the present analysis since there is no reflection back into the DFB cavity as a consequence of the grating tilt. Locations and widths of grating ridge/groove segments in all the cycles in this cavity are calculated, assuming a 50% duty cycle. This chirped grating along the defined laser cavity is converted to a multi-layer stack structure with layer locations and thicknesses corresponding to the grating ridge/groove segments previously found. An overall cavity transfer matrix is then constructed using all the interface and translation matrices describing the different individual layers along the cavity,

following the standard TMM procedure (Fig. 8). Because of the hyperbolically chirped grating patterned on the device, incident/transmitted angles appearing in the Fresnel relations in the evaluation of the components of the interfaces matrices and propagation angles in the phase terms of the translation matrices are not 90° , and the resulting optical path is not a straight line. The optical path centerline is found through iterative optimization, and the transfer matrices for each path segment and each interface are calculated individually. Considering the grating line orientation variation along the cavity (pump stripe) is on the order of only 1° , this procedure to calculate the angles and optical path is straightforward. The equation used to calculate the angles on interfaces is given in equation (3).

$$\phi = \sin^{-1} \left(\frac{\tilde{n}_{eff,R} \sin \theta}{\tilde{n}_{eff,G}} \right) = -i \ln \left[i \left(\frac{\tilde{n}_{eff,R} \sin \theta}{\tilde{n}_{eff,G}} \right) + \sqrt{1 - \left(\frac{\tilde{n}_{eff,R} \sin \theta}{\tilde{n}_{eff,G}} \right)^2} \right], \quad (3)$$

where θ and ϕ are incident and transmitted angles on the interface, $\tilde{n}_{eff,R}$ and $\tilde{n}_{eff,G}$ are the complex effective refractive indices for the ridge and groove portions of the structure, respectively.

For a parabolic grating chirp in the longitudinal direction, the results for the transmission and reflection of the grating structure are shown in Fig. 9. For an unchirped grating the traditional symmetrical passband curve is obtained. The FWHM of the stop-band, which in this low coupling regime is proportional to $|n_{eff,R} - n_{eff,G}| / \bar{n}_{eff}$, is $\sim 0.024\%$. For the chirped grating with a 0.01% longitudinal chirp, comparable

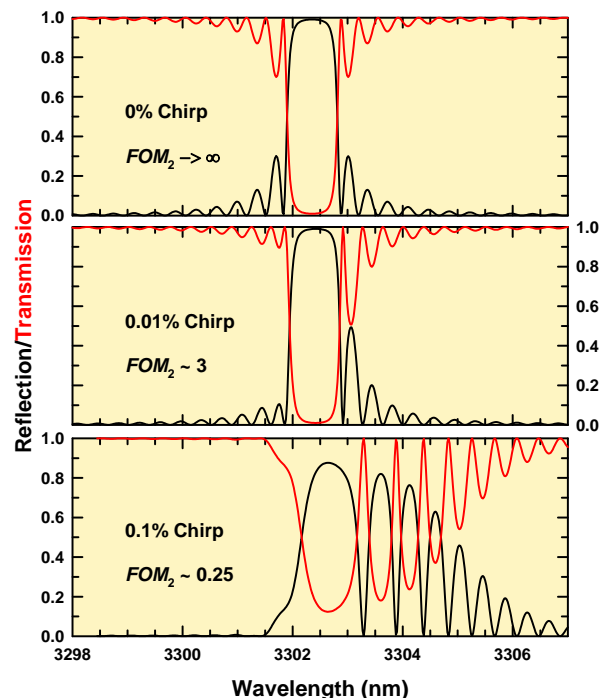


Fig. 9. Reflection/transmission for DBR sections ($\kappa L = 3$) showing the effects of longitudinal chirp.

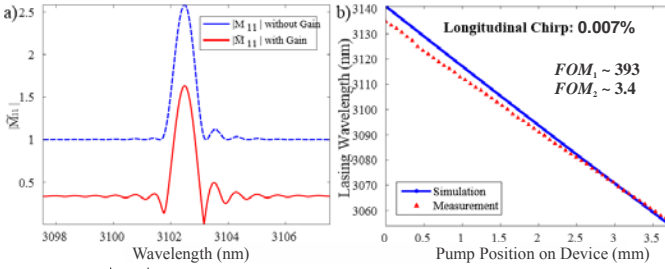


Fig. 10. (a) $|\tilde{M}_{11}|$ as a function of wavelength for a cold cavity (blue, no gain) and for a cavity with gain (red) showing the determination of the lasing wavelength. (b) The tuning curve generated by repeating this calculation as the pump stripe is translated along the device (blue line). The red dots are the measured lasing wavelengths.

to the FWHM, the strength of the reflection peak is decreased, and the sidebands become asymmetric showing more modulation at long wavelengths. The chirp in these calculations is to higher periods, or longer wavelengths; for the opposite chirp, the asymmetry is reversed as expected. At a chirp of 0.1%, considerably broader than the unchirped FWHM, the DBR characteristic becomes a series of resonances with a slowly decreasing envelope. The wavelength spacing of these resonances increases as the chirp increases. As shown below, these resonances are the source of the mode hops observed when tuning a device with a chirp on this order.

In the cavity transfer matrix construction, the fractional grating cycles disappear together with the output medium for the grating normal configuration because the reflection from the facets is not directed back into the cavity. This simplifies the procedure of cavity transfer matrix construction and eliminates the random phases at facets due to cleaving. With the real effective refractive indices in the previous calculation steps replaced by complex indices representing optical gain, transmittance and reflectance curves of the laser cavity within the wavelength tuning range are calculated using the transfer matrix. The laser cavity transfer matrix can be written as a 2×2 matrix as shown in Eq. (4):

$$\begin{pmatrix} 0 \\ R \end{pmatrix} = \begin{pmatrix} \tilde{M}_{11} & \tilde{M}_{12} \\ \tilde{M}_{21} & \tilde{M}_{22} \end{pmatrix} \begin{pmatrix} T \\ 0 \end{pmatrix} \quad (4)$$

Finally, the imaginary part of the refractive index in the gain medium is increased in small steps until the oscillation condition $|\tilde{M}_{11}| = 0$, which corresponds to the physical situation where the device has outputs R and T in the absence of an input [39] is reached; the corresponding wavelength is taken as the lasing wavelength. A plot of $|\tilde{M}_{11}|$ as an example of the lasing wavelength solution at an arbitrary pump stripe location on device is shown in Fig. 10(a) and the tuning curve obtained by translation of the pump stripe along the device is shown in Fig. 10(b). There is reasonable agreement between the measurement and the calculation, given the uncertainties in the precise variation of the grating period across the device. As in the experiment, the model shows no evidence of mode

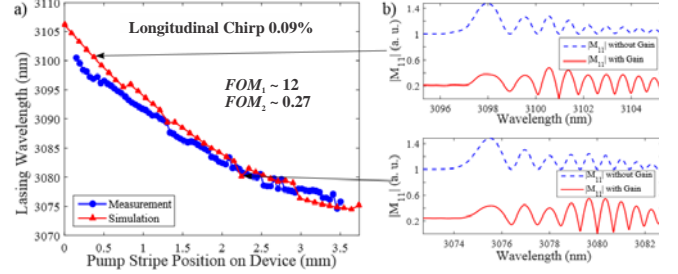


Fig. 11. (a) Simulated tuning curve (red) and experimental result (blue) for a device with the same epitaxial structure but with a grating with a ten times larger longitudinal chirp. The mode hops are evident in both the model and the experiment. (b) Two $|\tilde{M}_{11}|$ plots; the top one corresponds to a position away from mode hops, while the bottom one is close to a mode-hop region. Note that there are several nearly equivalent minima in the plot which change relative strengths with small changes in the position.

hopping throughout the tuning range.

This model was also tested on the high-chirp DFB laser device with a $10 \times$ larger longitudinal chirp that had exhibited clear mode hopping behavior [24]. Both the tuning behavior and the existence of mode hopping were displayed, as shown in Fig. 11. $|\tilde{M}_{11}|$ plots at two particular pump strip positions are also shown for the cases one in a region of relative mode stability, and one close to a mode hop regime. Using the same model, wavelength tuning range of the present tunable DFB laser device is plotted by solving the lasing wavelengths at a series of different pump stripe positions across the whole lateral width of the device, as shown in the blue curve in the Fig. 11(b). So this model provides indirect proof that our low-chirp DFB laser device is continuously tuned without mode hops. This result greatly increases our confidence in the tuning results shown in Fig. 10 and codifies the importance of the longitudinal chirp in mode hopping behavior for this chirped grating device.

V. CONCLUSION

A novel method to pattern a hyperbolically chirped grating using interference between two spherical waves with precise control on longitudinal/lateral chirp was developed and demonstrated with an optically pumped tunable index coupled DFB laser fabricated. A 4×2.5 mm laser device with grating period range of 410 to 420 nm shows a continuous, mode-hop-free, wavelength tuning range of 80 nm from 3057 to 3137 nm at $2.5 \times$ threshold pump power. The single facet output power of this DFB laser device reaches 820 mW limited only by the available pump power. Spectral linewidth at $\sim 2.5 \times$ threshold is typically 1.2 nm, reflecting multi-transverse mode operation of this gain guided laser, sufficient for application of remote gas sensing at atmospheric pressure. F-P modes were successfully suppressed with tilting the grating orientation relative to laser facets and a grating normal pump stripe configuration.

The importance of reducing the longitudinal chirp of the grating has been emphasized. This chirp leads to a walk-off of the DFB mode from the DFB structure and lowers the coupling and leads to mode jumps that interfere with continuous tuning. The important parameter is the chirp relative to the

DFB stop-band bandwidth.

With a larger die tilt angle in IL, the lateral chirp of grating could be further increased with even lower longitudinal chirp which is ideal especially for wavelength tuning purposes. A tunable range of over 100 nm should be feasible for a 4 mm long DFB laser device. Practical values of β in IL need to be determined in future work. Another option for even wider wavelength tuning range will be to cascade different laser devices, to take full advantage of the gain medium bandwidth.

ACKNOWLEDGMENT

This work was supported in part by the Defense Threat Reduction Agency, the Air Force Office of Scientific Research, and the Army Research Office, under an SBIR grant to Southwest Sciences, Inc.

REFERENCES

- [1] C. Gmachl, R. Kohler, F. Capasso, A. Tredicucci, A. L. Hutchinson, D. L. Sivco, J. N. Baillargeon and A. Y. Cho, "Single-mode, tunable quantum cascade distributed feedback (QC-DFB) lasers between 4.6 and 10 μm wavelength," in *CLEO 2000, volume CWF1, page 264*, 2000.
- [2] C. J. Chang-Hasnain, "Tunable VCSEL," *IEEE J. Select. Optics Quantum Electron.*, vol. 6, no. 6, pp. 978-987, Nov. 2000.
- [3] S. Suchalkin, M. Kisin, S. Luryi, G. Belenky, F. Towner, J. D. Bruno, C. Monroy and R. L. Tober, "Wavelength tuning of interband cascade lasers based on Stark effect," *Future Trends in Microelectronics*, John Wiley & Sons, Inc., 2007, pp. 369-379.
- [4] S. Suchalkin, M. V. Kisin, S. Luryi, G. Belenky, F. Towner, J. D. Bruno and R. Tober, "High-Speed Stark Wavelength Tuning of MidIR Interband Cascade Lasers," *Photonics Technology Letters, IEEE*, vol. 19, no. 6, pp. 360-362, 2007.
- [5] Y. Jiang, L. Li, Z. Tian, H. Ye, L. Zhao, R. Q. Yang, T. D. Mishima, M. B. Santos, M. B. Johnson and K. Mansour, "Electrically widely tunable interband cascade Lasers," *Journal of Applied Physics*, vol. 115, p. 113101, 2014.
- [6] M. Ito and T. Kimura, "Oscillation properties of AlGaAs DH lasers with an external grating," *IEEE Journal of Quantum Electronics*, vol. 16, pp. 69-77, 1980.
- [7] B. Glance, C. A. Burrus and L. W. Stulz, "Fast frequency-tunable external cavity laser," *Electron. Lett.*, vol. 23, pp. 98-100, 1987.
- [8] R. Maulini, A. Mohan, M. Giovannini, J. Faist and E. Gini, "External cavity quantum-cascade laser tunable from 8.2 μm to 10.4 μm using a gain element with a heterogeneous cascade," *Appl. Phys. Lett.*, vol. 88, p. 201113, 2006.
- [9] G. Wysocki, R. Lewicki, R. F. Curl, F. K. Tittel, L. Diehl, F. Capasso, M. Troccoli, G. Hofler, D. Bour, S. Corzine, R. Maulini, M. Giovannini and J. Faist, "Widely tunable mode-hop free external cavity quantum cascade lasers for high resolution spectroscopy and chemical sensing," *Applied Physics B*, vol. 92, no. 3, pp. 305-311, 2008.
- [10] A. Hugi, R. Terazzi, Y. Bonetti, A. Wittmann, M. Fischer, M. Beck, J. Faist and E. Gini, "External cavity quantum cascade laser tunable from 7.6 μm to 11.4 μm ," *Appl. Phys. Lett.*, vol. 95, p. 061103, 2009.
- [11] V. Jayaraman, A. Mathur, L. A. Coldren and P. D. Dapkus, "Very wide tuning range in sampled grating DBR laser," in *13th IEEE Laser Conf.* '92, 1992.
- [12] V. Jayaraman, D. A. Cohen and L. A. Coldren, "Extended tuning range in a distributed feedback InGaAsP laser with sampled gratings," in *OFC'92*, 1992.
- [13] S. Kim, Y. Chung, S.-H. Oh and M.-H. Park, "Design and analysis of widely tunable sampled grating DFB laser diode integrated with sampled grating distributed Bragg reflector," *IEEE Photon. Technol. Lett.*, vol. 16, no. 1, pp. 15-17, 2004.
- [14] B. Mason, G. Fish, S. DenBaars and L. Coldren, "Ridge waveguide sampled grating DBR lasers with 22-nm quasi-continuous tuning range," *IEEE Photonics Technology Letters*, vol. 10, no. 9, pp. 1211-1213, 1998.
- [15] Y. Tohmori, Y. Yoshikuni, H. Ishii, F. Kano, T. Tamamura, Y. Kondo and M. Yamamoto, "Broad-Range Wavelength-Tunable Superstructure Grating (SSG) DBR Lasers," *IEEE Journal of Quantum Electronics*, vol. 29, no. 6, pp. 1817-1823, 1993.
- [16] Y. Tohmori, F. Kano, H. Ishii, Y. Yoshikuni and Y. Kondo, "Wide tuning with narrow line width in DFB lasers with superstructure grating (SSG)," *Electron. Lett.*, vol. 29, pp. 1350-1352, 1993.
- [17] H. P. Gauggel, H. Artmann, C. Geng, F. Scholz and H. Schweizer, "Wide-range tunability of GaInP-AlGaInP DFB lasers with superstructure gratings," *IEEE Photon. Technol. Lett.*, vol. 9, pp. 14-16, 1997.
- [18] I. A. Avrutsky, D. S. Ellis, A. Tager, H. Anis and J. M. Xu, "Design of widely tunable semiconductor lasers and concept of binary superimposed gratings (BSG's)," *IEEE J. Quantum Electron.*, vol. 34, pp. 729-741, 1998.
- [19] B. G. Lee, M. A. Belkin, R. Audet, J. MacArthur, L. Diehl, C. Pflügl, F. Capasso, D. C. Oakley, D. Chapman, A. Napoleone, D. Bour, S. Corzine, G. Höfler and J. Faist, "Widely tunable single-mode quantum cascade laser source for mid-infrared spectroscopy," *Appl. Phys. Lett.*, vol. 91, p. 231101, 2007.
- [20] B. Pezeshki, E. Vail, J. Kubicky, G. Yoffe, S. Zou, J. Heanue, P. Epp, S. Rishton, D. Ton, B. Faraji, M. Emanuel, X. Hong, M. Sherback, V. Agrawal, C. Chipman and T. Razazan, "20-mW widely tunable laser module using DFB array and MEMS selection," *Photon. Technol. Lett.*, vol. 14, no. 10, pp. 1457-1459, 2002.
- [21] Y.-D. Chung, J.-S. Sim, S.-B. Kim, J. Kim, and S.-W. Ryu "Wavelength-selectable 8-channel WDM optical transmitter," *JKPS*, vol. 45, no. 3, pp. 605-608, 2004.
- [22] S. Bao, Y. Xi, S. Zhao and X. Li, "Sampled grating DFB laser array by periodic injection blocking," *IEEE J. Selected Topics in Quantum Electron.*, vol. 19, no. 5, pp. 1-8, 2013.
- [23] L. Xue, S. R. J. Brueck and R. Kaspi, "High-power continuous-wave single-longitudinal-mode operation of an optical pumped DFB laser at $\lambda \sim 3.64 \mu\text{m}$," *IEEE Photon. Technol. Lett.*, vol. 20, no. 9, pp. 727-729, 2008.
- [24] L. Xue, S. R. J. Brueck and R. Kaspi, "Widely tunable distributed-feedback lasers with chirped gratings," *Appl. Phys. Lett.*, vol. 94, p. 161102, 2009.
- [25] S. Benoit, Xiang He, R. Kaspi and S. R. J. Brueck, in preparation
- [26] L. A. Coldren, S. W. Corzine and M. L. Mašanović, *Diode Lasers and Photonic Integrated Circuits*, 2nd ed., Hoboken, New Jersey: John WILEY & Sons, Inc., 2012.
- [27] H. Ghafouri-Shiraz, *Distributed Feedback Laser Diodes and Optical Tunable Filters*, The Atrium, Souther Gate, Chichester, West Sussex, England: John Wiley & Sons Ltd, 2003.
- [28] T. Makino and J. Glineski, "Transfer matrix analysis of the amplified spontaneous emission of DFB semiconductor laser amplifiers," *IEEE J. Quantum Electron.*, vol. 24, no. 8, pp. 1507-1518, 1988.
- [29] T. Makino, "Transfer-matrix formulation of spontaneous emission noise of DFB semiconductor lasers," *J. Lightwave Technol.*, vol. 9, no. 1, pp. 84-91, 1991.
- [30] J. Hong, W. Huang and T. Makino, "On the transfer matrix method for distributed-feedback waveguide devices," *J. Lightwave Technol.*, vol. 10, no. 12, pp. 1860-1868, 1992.
- [31] S. Hansmann, "Transfer matrix analysis of the spectral properties of complex distributed feedback laser structures," *IEEE J. Quantum Electron.*, vol. 28, no. 11, pp. 2589-2595, 1992.
- [32] T. Makino, "Transfer-matrix theory of modulation and noise of multi-element semiconductor lasers," *IEEE J. Quantum Electron.*, vol. 29, no. 11, pp. 2762-2770, 1993.
- [33] T. Makino, "Threshold condition of DFB semiconductor lasers by the local-normal-mode transfer-matrix method: Correspondence to the coupled-wave method," *J. Lightwave Technol.*, vol. 12, no. 12, pp. 2092-2099, 1994.
- [34] T. Makino, H. Lu and G. P. Li, "Transfer-matrix dynamic model of partly gain-coupled 1.55 μm DFB lasers with a strained-layer MQW active grating," *IEEE J. Quantum Electron.*, vol. 30, no. 11, pp. 2443-2448, 1994.
- [35] T. Makino, "Transfer matrix method with applications to distributed feedback optical devices," *Progress In Electromagnetics Research*, vol. 10, pp. 271-319, 1995.
- [36] D. N. Maywar and G. P. Agrawal, "Transfer-matrix analysis of optical bistability in DFB semiconductor laser amplifiers with nonuniform gratings," *IEEE J. Quantum Electron.*, vol. 33, no. 11, pp. 2029-2037, 1997.
- [37] P. Verly, R. Tremblay and J. W. Y. Lit, "Application of the effective-index method to the study of distributed feedback in corrugated

waveguides. TE polarization," *J. Opt. Soc. Amer.*, vol. 70, no. 8, pp. 964-968, 1980.

[38] J. Buus, "The effective index method and its application to semiconductor lasers," *IEEE J. Quantum Electron.*, vol. 18, no. 7, pp. 1083-1089, 1982.

[39] M. Yamada and K. Sakuda, "Analysis of almost-periodic distributed feedback slab waveguides via a fundamental matrix approach," *Appl. Opt.*, vol. 26, no. 16, pp. 3474-3478, 1987.

1.

1. Report Type

Final Report

Primary Contact E-mail

Contact email if there is a problem with the report.

sbrueck@unm.edu

Primary Contact Phone Number

Contact phone number if there is a problem with the report

505-272-7800

Organization / Institution name

Regents of the University of New Mexico

Grant/Contract Title

The full title of the funded effort.

Unstable Resonator Mid-Infrared Laser Sources

Grant/Contract Number

AFOSR assigned control number. It must begin with "FA9550" or "F49620" or "FA2386".

FA9550-12-1-0480

Principal Investigator Name

The full name of the principal investigator on the grant or contract.

Steven R. J. Brueck

Program Manager

The AFOSR Program Manager currently assigned to the award

Dr. John Luginsland

Reporting Period Start Date

09/30/2012

Reporting Period End Date

09/29/2015

Abstract

Progress has been made in tunable infrared lasers and in novel epitaxial structures for next generation electronics. A tunable infrared laser based on a chirped grating distributed feedback structure and optical pumping has been demonstrated with an 80-nm tuning range at 3.1 micron and a linewidth of < 1 nm. Novel nanowire geometries based on selective growth of heterogeneous materials on Si(001) substrates have been designed and initial demonstrations of growth have been undertaken.

Distribution Statement

This is block 12 on the SF298 form.

Distribution A - Approved for Public Release

Explanation for Distribution Statement

If this is not approved for public release, please provide a short explanation. E.g., contains proprietary information.

SF298 Form

Please attach your [SF298](#) form. A blank SF298 can be found [here](#). Please do not password protect or secure the PDF. The maximum file size for an SF298 is 50MB.

[final_report_AFOSR_298.pdf](#)

Upload the Report Document. File must be a PDF. Please do not password protect or secure the PDF . The maximum file size for the Report Document is 50MB.

[final_report_AFOSR.pdf](#)

Upload a Report Document, if any. The maximum file size for the Report Document is 50MB.

Archival Publications (published) during reporting period:

Xiang He, S. Benoit, R. Kaspi and S. R. J. Brueck
Optically-Pumped Continuously-Tunable Mid-IR Distributed-Feedback Semiconductor Laser
Submitted to IEEE Journal of Quantum Electronics

S. Benoit, Xiang He and S. R. J. Brueck
Controlled Chirp Gratings Fabricated by Interferometric Lithography
in preparation

Changes in research objectives (if any):

Initial objectives were to fund unstable resonator research involving the Air Force Research Laboratory. Personnel changes led to work on tunable lasers in collaboration with AFRL. Additional work was undertaken in next-generation transistors based on ongoing work at UNM.

Change in AFOSR Program Manager, if any:

Change from Dr. Howard Schlossberg to Dr. John Luginsland.

Extensions granted or milestones slipped, if any:

None.

AFOSR LRIR Number

LRIR Title

Reporting Period

Laboratory Task Manager

Program Officer

Research Objectives

Technical Summary

Funding Summary by Cost Category (by FY, \$K)

	Starting FY	FY+1	FY+2
Salary			
Equipment/Facilities			
Supplies			
Total			

Report Document

Report Document - Text Analysis

Report Document - Text Analysis

Appendix Documents

2. Thank You

E-mail user

Feb 16, 2016 13:02:23 Success: Email Sent to: sbrueck@unm.edu